A dynamic mid-crustal magma domain revealed by the 2023-24 Sundhnúksgígar eruptions, Iceland

Authors: Simon W. Matthews[1]*, Alberto Caracciolo[1], Enikő Bali[1], Sæmundur A. Halldórsson[1], Olgeir Sigmarsson[1,2], Guðmundur H. Guðfinnsson[1], Gro B. M. Pedersen[1,3], Jóhann Gunnarsson Robin[1], Edward W. Marshall[1,4], Araksan A. Aden[1], Bryndís Ýr Gísladóttir[1], Chantal Bosq[2], Delphine Auclair[2], Heini Merrill[1], Nicolas Levillayer[1], Noëmi Löw[1], Rebekka Hlín Rúnarsdóttir[1], Sóley M. Johnson[1], Sveinbjörn Steinþórsson[1], Vincent Drouin[3]

Affiliations:

[1]Nordic Volcanological Centre, Institute of Earth Sciences, University of Iceland; Reykjavík, Iceland.
[2]Laboratoire Magmas et Volcans, Université Clermont Auvergne; Aubière, France.
[3]Icelandic Meteorological Office, Reykjavík, Iceland
[4]GeoZentrum Nordbayern, Friedrich-Alexander-Universität Erlangen-Nürnberg; Erlangen, Germany

*Corresponding author. Email: simonm@hi.is

Abstract: Mid-crustal magma domains are the source of many basaltic eruptions. Lavas from individual eruptions are often chemically homogeneous, suggesting they derive from single well-mixed magma reservoirs. The 2023-2024 eruptions at Sundhnúksgígar in the Svartsengi volcanic system, Iceland, provide an opportunity to observe the behavior of a mid-crustal magma domain at high spatial and temporal resolution by detailed sampling and geochemical characterization. We observed substantial mantle-derived geochemical variability in the products erupted in the first hours of the December 2023, January, February, and March-May 2024 eruptions, indicating the eruptions derived from multiple magma reservoirs, which mineral-melt equilibration pressures place in the mid-crust. The unusual presence of geochemical heterogeneity in the mid-crustal magma domain provides an insight into how dynamic and complex mid-crustal magma domains can be.

One-Sentence Summary: Chemical variability in consecutive eruptions at Svartsengi, Iceland, reveals a complex and dynamic mid-crustal magma domain

Main Text:

Basaltic eruptions at ocean islands and mid-ocean ridges are often fed from magma storage domains in the mid to shallow crust (*1-4*). The products erupted during these events are generally chemically homogeneous (*3, 5-8*), leading to the assumption that the last stage of pre-eruptive magma accumulation occurs in a single reservoir (*2, 9, 10*) when modelling volcanic behavior (*11-13*) and assessing hazard from real-time geophysical monitoring (*14-16*). A sequence of eruptions beginning in December 2023 at the Sundhnúksgígar crater row in the Svartsengi volcanic system, Reykjanes, Iceland, provided an opportunity to test this model; the patterns of ground deformation preceding eruption indicated magma accumulation in a mid-crustal magma domain ~5 km below the surface (*15, 17*). The presence of chemically heterogeneous melts in magma reservoirs close to the crust-mantle boundary (Moho) at ~16 km depth (*18*) was shown by the 2021 eruption in the neighboring Fagradalsfjall complex (*19*), suggesting that chemically variable melts have also ascended towards the mid-crustal magma domain beneath Svartsengi. If the magma domain is characterized by a single, or well-connected set, of magma reservoirs then chemical variability ought to be rapidly homogenized.

To examine the nature of the Svartsengi magma domain, we sampled lava and tephra from four eruptions between December 2023 and May 2024, with high spatial and temporal resolution. By characterizing the petrology and geochemistry, including the major and trace element concentrations, $^{87}Sr/^{86}Sr$ and $^{143}Nd/^{144}Nd$ isotope ratios, and mineral compositions, we constrain the depths of pre-eruptive magma storage, the configuration of the magma domain, and its changing behavior throughout the eruptive events. While our observations provide insights into the operation of mid-crustal magma domains globally, they also have implications for understanding and predicting the behavior of the ongoing volcanic crisis at Svartsengi.

Volcanic unrest on Reykjanes since 2020

Following a hiatus of ~780 years (*9, 20*), volcanic and tectonic unrest on Reykjanes began with seismicity close to Svartsengi in January 2020, accompanied by inflation at ~4 km beneath the Svartsengi and Krýsuvík geothermal fields (*17*) (Fig 1A). Inflation continued episodically at Svartsengi until continuous inflation started in late 2023 (*15*). Following a dike intrusion beneath the Fagradalsfjall complex in early 2021, a volcanic eruption began there in March 2021 (*21*). This eruption continued until September 2021 (*22*), and was followed by two shorter eruptions in 2022 and 2023 (*16, 23*).

The composition of the material erupted during the first 40 days of the 2021 Fagradalsfjall eruption displayed a shift in mantle-derived parameters (e.g., K_2O/TiO_2, La/Yb, and radiogenic isotopes) from depleted to enriched values (*19, 24*)., and geobarometry indicated the magmas were transported directly from near the Moho (*19*).The eruption of such large amplitude mantle-derived heterogeneity in a single event was unique, but consistent with the presence of diverse mantle melts in near-Moho magma reservoirs as inferred from the melt inclusion and mineral record (*25, 26*).

Inflation resumed beneath the Svartsengi geothermal field in late 2023, centered on a depth of ~5 km (*15*). On 10 November, a large dike intrusion occurred beneath the Sundhnúksgígar crater row (last active ~2400 years ago) (*27*), propagating beneath Grindavík, and off the southern coast (*15*). Inflation continued beneath Svartsengi, and an eruption began on 18 December 2023 lasting until 21 December 2023, along the northern part of the Sundhnúksgígar crater row (Fig. 1B). A second eruption occurred on 14 January 2024 along

the southernmost part of the Sundhnúksgígar crater row, and a second fissure opened a few hours later further to the South, close to the edge of Grindavík (Fig. 1C). The eruption ended on 16 January 2024. A third eruption occurred on 8 February 2024 along a fissure slightly offset from the December fissure (Fig. 1D) and ended after one day. A fourth eruption began on 16 March 2024, continuing until 9 May 2024 (Fig. 1E), along a fissure close to that of February. Inflation beneath Svartsengi resumed in April 2024.

Rapid changes in the composition of erupted magmas

We obtained samples of lava and tephra throughout the eruptions and additional material was collected after the end of each eruption, ensuring good spatial and temporal coverage (Fig. 1). All the erupted material is tholeiite basalt (fig. S1) and contains a variable crystal assemblage of olivine, plagioclase, clinopyroxene, and chromian spinel (*28*). In the glassy lava crusts a microlite assemblage exists and is dominated by olivine and plagioclase, while the tephra is microlite-poor (fig. S2). The samples show a large range in their major element oxide concentrations (Fig. 2A, fig. S3), and form a linear array between a low-MgO and -K_2O (depleted) endmember and a high-MgO and -K_2O (enriched) endmember. The scatter in composition about this array is consistent with variable proportions of accumulated crystals. Because the crystallizing assemblage does not contain substantial amounts of K_2O and TiO_2 (fig. S4), the K_2O/TiO_2 ratio is not affected by either fractional crystallization or crystal addition and resolves the two compositional endmembers clearly (Fig. 2B). The utility of K_2O/TiO_2 as a tracer insensitive to crystallization is further confirmed by the coincident variability in $^{87}Sr/^{86}Sr$ and $^{143}Nd/^{144}Nd$ isotope ratios (Fig. 2C, fig. S5) and incompatible trace element (ITE) ratios (fig. S5). The greatest variability in K_2O/TiO_2 was seen in the December and January products, while in the February products the range in K_2O/TiO_2 was much suppressed (Figs. 2B, D-F), though still analytically resolvable (fig. S6). Variability, while less than in December and January, returned at the beginning of the March – May eruption (Fig. 2G), though lavas emplaced after ~day 5 of this eruption were relatively homogeneous (fig. S7). A similar range of K_2O/TiO_2 is present in melt inclusions found in all four eruptions (fig. S8).

High magma effusion rates and intense fountaining occurred in the first hours of the December eruption, meaning that much of the areal extent of the lava was emplaced within this time (fig. S9), including flows that represent both enriched (high K_2O/TiO_2) and depleted (low K_2O/TiO_2) compositions. This timescale is orders of magnitude shorter than the 40 days over which a similarly large change in composition was observed at Fagradalsfjall in 2021 (*19*) (Fig. 2B,C). Tephra deposited early in the eruption has the most enriched composition, and the last lava lobes emplaced at the edge of the flow were depleted (*28*) (figs. S9C, S7A). Likewise, there was a general change from enriched to depleted compositions with time during the January, February, and March - May eruptions (fig. S7B,C,D).

Petrological constraints on pre-eruptive melt storage conditions

The depleted and enriched products contain distinct populations of clinopyroxene microphenocrysts, distinguished by their Mg# (fig. S10B), but the crystals are close to being in equilibrium with the glass compositions. Our pressure estimates were derived using the clinopyroxene-liquid barometer (*29*), using the glass compositions as potential equilibrium liquids for the microphenocryst core compositions, which give mean pressure estimates of 1.6 ± 1.4 kbar (5.4 ± 4.7 km) for crystals in the enriched products and 2.2 ± 1.4 kbar (7.2 ± 4.7 km) for crystals in the depleted products (Fig. 3A). Similar pressures are estimated

from the crystal rims, and small glomerocrysts (Fig. 3B, C). The presence of glomerocrysts containing olivine, plagioclase, and clinopyroxene (fig. S2E,F), suggests the magmas were three-phase saturated during pre-eruptive storage, a necessary condition for applying the OPAM geobarometer (*1, 10, 30*). The mean OPAM pressure estimate for the tephra glass is 1.24 ± 1.13 kbar (4.1 ± 3.8 km), distinct from the mean pressure estimated from the glassy lava crusts: 0.29±1.13 kbar (1.0 ± 3.8 km), which represents re-equilibration at surface pressures by microlite growth during eruption (Fig. 3D, fig S2). The clinopyroxene-liquid and tephra OPAM equilibration pressures are all within mutual uncertainty and point towards pre-eruptive magma storage in the mid-crust. The higher pressures recorded by some clinopyroxene crystals are consistent with some of the crystal cargo having formed in deeper reservoirs (*2, 10, 31*).

The mean OPAM temperature estimate for the tephra glass is 1166 ± 10˚C (fig. S11), ~60˚C lower than the OPAM temperature calculated from the 2021 Fagradalsfjall tephra (*19*), consistent with the lower MgO concentrations in the Sundhnúksgígar lavas (Fig. 2). Little change is seen in the MgO concentrations in the whole rocks and glasses between eruptions (Fig. 2, fig. S3), nor in the liquidus temperatures (fig. S12). This suggests the pre-eruptive storage region is not cooling substantially over the timescale of these eruptions; the magma storage region is likely at thermal equilibrium with the surrounding (more-refractory) gabbroic crust, with hotter intruding magmas quickly losing heat. Indeed, the high temperature geothermal field present in the shallow crust above the magma domain (separated by the brittle-ductile transition, Fig. 4) indicates a long-lived high temperature anomaly in the mid-crust (*17*).

Magma supply to the Svartsengi mid-crustal magma domain

The Sundhnúksgígar magmas define tight arrays in plots of ITE ratios and radiogenic isotope ratios (Fig. 2C, fig. S5), consistent with variable amounts of mixing between depleted and enriched endmember magmas. Relative to the Fagradalsfjall 2021 magmas, the Sundhnúksgígar magmas have slightly more radiogenic $^{87}Sr/^{86}Sr$ (Fig. 2C), and their ITE ratios are offset to more enriched values (figs. S5, S13). The offset in both ITE ratios and radiogenic isotopes requires that the mixing endmembers for the Sundhnúksgígar magmas have compositions distinct from Fagradalsfjall 2021 (*28*). Magmas erupted at Fagradalsfjall in 2022 and 2023 have $^{87}Sr/^{86}Sr$ intermediate between the enriched endmembers of Fagradalsfjall 2021 and Sundhnúksgígar (Fig. 2C). The shift in composition of mixing endmembers likely reflects the dynamic magma supply from the near-Moho magma storage region (*19*).

The composition of the Sundhnúksgígar depleted endmember sits between those of the enriched endmember and the lavas erupted at Svartsengi in previous eruptive cycles (*32*), and is similar, but not identical, to the depleted endmember seen at Fagradalsfjall (Fig. 2). Distinguishing whether the depleted endmember corresponds to magmas resident in the crust since the last eruptive cycle (800-1240 AD) or it represents a new influx of magma from near-Moho depths since unrest started in 2020 is difficult. Seismic evidence exists for the presence of magma in the mid-crust beneath Svartsengi before unrest started in 2020 (*33*), and the inferred volume of the November 2023 dike intrusion was larger than the cumulative volume increase associated with inflation between 2020 and 2023 (*15*), which might suggest the involvement of magmas accumulated long before 2020. On the other hand, depleted magmas were erupted almost directly from a near-Moho magma reservoir at Fagradalsfjall in 2021 (*19, 34*), a clear indication that depleted melts were present at depth and could ascend to shallower levels, at least in 2021. The trend towards more depleted compositions in the

March – May eruption further suggests depleted melts were being supplied to the magma domain throughout the eruptive episodes.

Though the Sundhnúksgígar magmas were not derived directly from the more primitive magmas erupted at Fagradalsfjall, the higher concentrations of K_2O, TiO_2, and the ITEs in the endmember melts at Sundhnúksgígar (Fig. 2A, figs. S5, S13) are most likely due to fractional crystallization of the magmas, with concentrations in the parental melts being only subtly different. Based on this, the depleted endmember at Sundhnúksgígar underwent ~46% additional crystallization relative to the depleted endmember at Fagradalsfjall (*28*), and the enriched endmember underwent an additional ~35% crystallization, consistent with experiments and modelling performed on endmember Reykjanes Peninsula magma compositions (*35*). The Sundhnúksgígar magmas being more evolved than the Fagradalsfjall magmas is consistent with the ~60˚C lower OPAM temperature estimated from the Sundhnúksgígar tephra than the Fagradalsfjall tephra (*19*).

A dynamic magma domain beneath Svartsengi

When two basaltic magmas are present in a convecting reservoir, magma mixing and homogenization is expected to be rapid, within days to weeks (*36, 37*). In the Sundhnúksgígar products, the presence of crystals that are close to being in equilibrium with the matrix glass, or are more primitive (fig. S10), suggests crystallization, and therefore cooling coupled with convective circulation, was occurring in the pre-eruptive storage region. Prior to the December and January eruptions the endmember magmas were likely isolated from each other (in the mid-crust) until immediately before eruption, then mixed incompletely either in one reservoir or during ascent (Fig. 4). This suggestion is further supported by the distinct populations of clinopyroxene core compositions in the depleted and enriched material (fig. S10B), and the presence of skeletal olivine and plagioclase crystals (fig. S2), likely indicating rapid growth following magma mixing (*38*). The similarity in the amplitude of chemical heterogeneity between the December and January eruptions further suggests that they were not supplied from a single reservoir that was becoming homogenized with time. The eruption of lava and tephra with intermediate K_2O/TiO_2 within the first hours of eruption (fig. S7) is consistent with rapid mixing during transport to the surface (Fig. 4).

The lava and tephra erupted in February have a much tighter range of K_2O/TiO_2 (Fig. 2F), consistent with this eruption being fed from a single almost-homogeneous magma reservoir. The small variability in K_2O/TiO_2 that is present (fig. S6) suggests that magma mixing may have occurred in the days or weeks prior to the eruption (*37*). Whether mixing took place in the same reservoirs that supplied the December and January eruptions, or this was a separate, but nearby, reservoir is unclear. The reemergence of heterogeneity at the beginning of the March eruption suggests either that homogenization did not affect the entire domain, or melts of a distinct composition continued to arrive from deeper reservoirs. Together, the observations from the four eruptions suggest that a minimum of two isolated reservoirs were present in the mid-crust beneath Svartsengi and were able to contribute magmas to the eruptions (near) simultaneously. Furthermore, the changing amplitude of geochemical variability present in the eruptions demonstrates either that successive eruptions may not be derived from the same reservoir(s), or that the reservoirs are dynamic, i.e., they are not in a steady state.

Contributions from multiple magma reservoirs to the flux out of the mid-crustal magma domain may also explain the difference in the geometry of geodetic signals before and after the November 2023 diking event. While the inflation was well matched by a sill-like source,

the deflation was best modelled with a spherical source, potentially a result of magma extraction from multiple reservoirs at different depths (*15*). Rather than being driven primarily by magma chamber overpressure, the November 2023 diking event is thought to have been precipitated by tectonic stress (*15*), aiding the contribution of multiple magma reservoirs. It is possible that residual tectonic stress continued to play a role in the subsequent eruptions, enabling them to tap multiple magma reservoirs simultaneously. However, pressure changes arising within individual magma reservoirs can cause magma to be mobilized from nearby reservoirs (*39*).

Implications for mid-crustal magma domains

A mid-crustal magma domain preserving geochemical heterogeneity, probably in multiple isolated reservoirs, is a unique observation for Iceland, where mid-crustal basaltic reservoirs are generally devoid of geochemical heterogeneity (*25, 37*). However, few lava fields have been sampled at a comparable resolution, and samples from the earliest phases of an eruptive episode are not available for most ancient lava units. It is therefore possible that the appearance of geochemical heterogeneity is a result of sampling bias. The Borgarhraun lava field in Northern Iceland is an example of an ancient lava flow, erupted directly from near-Moho depths, where detailed sampling has revealed substantial geochemical heterogeneity (*40*). While the amplitude of chemical heterogeneity is muted in Borgarhraun compared with Sundhnúksgígar and Fagradalsfjall, it demonstrates that heterogeneity can be found even when the earliest products are covered by later erupted lavas.

Elsewhere, the presence of substantial mantle-derived geochemical heterogeneity has been inferred for the shallow magma reservoirs beneath Kīlauea and the East Pacific Rise (EPR). At Kīlauea, lavas erupting between 1971 and 1982 defined bimodal trends in radiogenic Pb isotope ratios, corresponding to different parts of the eruptive fissure (*41*). Though this was indicative of two distinct shallow reservoirs contributing to the eruptions, the magmas remained separated from each other, unlike Sundhnúksgígar where they could partially mix during ascent. At a fast-spreading segment on the EPR, high-resolution sampling has revealed mantle-derived heterogeneity within a single mapped unit (*42*), albeit with a smooth variation occurring on a much larger wavelength than at Sundhnúksgígar (> 10 km). Though the chemical diversity was likely erupted during different events (*43*), the persistence of axial magma reservoirs (*44*) means that the heterogeneity is most likely present within the shallow magma domain. Despite their differences to Sundhnúksgígar, both of these examples demonstrate that mantle-derived heterogeneity can be present in the mid-crust and multiple magma reservoirs can contribute to single eruptive episodes.

In contrast to basaltic eruptions, eruptions involving more silicic magmas are well established to often be sustained from multiple magma reservoirs, whose configuration can change throughout the course of an eruption (*45-47*). Like the rare examples from basaltic eruptions above, the contribution of multiple magma reservoirs has been identified from geochemical variability in the erupted material. However, this variability is seldom mantle-derived, instead being generated in situ by variable extents of cooling and assimilation of country rock (*48, 49*). If the contribution of multiple basaltic reservoirs is only revealed on the occasion that mantle-derived heterogeneity escapes homogenization at depth and propagates to the mid-crust, it follows that the role of multiple reservoirs has been underestimated in basaltic eruptions derived from mid-crustal magma domains.

Finally, the observations at Sundhnúksgígar provide further constraints on how the signal of mantle compositional heterogeneity is modulated and diminished by the crust (*44*). In

magmatic systems in Iceland, basaltic melts are largely homogenized in near-Moho magma reservoirs, before ascending to shallower levels (*25, 37*). Where mantle-derived heterogeneity has been seen in single flow units or eruptions in Iceland, the magmas have been derived directly from the near the Moho (*6, 19, 40*). As discussed above, observations at mid-ocean ridges (*42, 44*), Hawai'i (*41*), and now Sundhnúksgígar, demonstrate that occasionally this heterogeneity can propagate into shallower magma domains. In some cases (e.g., the reservoir feeding the February eruption) this heterogeneity may be homogenized in the mid-crust, but it seems that basaltic magmas are in general unlikely to continue homogenizing here, and instead reside in largely isolated magma reservoirs.

References and Notes

1. R. J. M. Baxter, J. Maclennan, D. A. Neave, T. Thordarson, Depth of Magma Storage Under Iceland Controlled by Magma Fluxes. *G3* **24**, (2023).
2. D. A. Neave, E. Passmore, J. Maclennan, G. Fitton, T. Thordarson, Crystal–Melt Relationships and the Record of Deep Mixing and Crystallization in the ad 1783 Laki Eruption, Iceland. *JPet* **54**, 1661-1690 (2013).
3. S. A. Halldórsson *et al.*, Petrology and geochemistry of the 2014–2015 Holuhraun eruption, central Iceland: compositional and mineralogical characteristics, temporal variability and magma storage. *CMP* **173**, (2018).
4. K. V. Cashman, R. S. Sparks, J. D. Blundy, Vertically extensive and unstable magmatic systems: A unified view of igneous processes. *Science* **355**, (2017).
5. E. Passmore, J. Maclennan, G. Fitton, T. Thordarson, Mush Disaggregation in Basaltic Magma Chambers: Evidence from the ad 1783 Laki Eruption. *JPet* **53**, 2593-2623 (2012).
6. J. Sinton, K. Grönvold, K. Saemundsson, Postglacial eruptive history of the Western Volcanic Zone, Iceland. *G3* **6**, Q12009 (2005).
7. D. E. Eason, J. M. Sinton, Lava shields and fissure eruptions of the Western Volcanic Zone, Iceland: Evidence for magma chambers and crustal interaction. *Journal of Volcanology and Geothermal Research* **186**, 331-348 (2009).
8. O. Sigmarsson, M. Condomines, K. Grönvold, T. Thordarson, Extreme magma homogeneity in the 1783–84 Lakagigar Eruption: Origin of a large volume of evolved basalt in Iceland. *Geophysical Research Letters* **18**, 2229-2232 (1991).
9. A. Caracciolo *et al.*, Magma plumbing architectures and timescales of magmatic processes during historical magmatism on the Reykjanes Peninsula, Iceland. *EPSL* **621**, (2023).
10. M. E. Hartley, E. Bali, J. Maclennan, D. A. Neave, S. A. Halldorsson, Melt inclusion constraints on petrogenesis of the 2014-2015 Holuhraun eruption, Iceland. *Contrib Mineral Petrol* **173**, 10 (2018).
11. M. T. Gudmundsson *et al.*, Gradual caldera collapse at Barðarbunga volcano, Iceland, regulated by lateral magma outflow. *Science* **353**, aaf8988 (2016).
12. F. Galetto, V. Acocella, A. Hooper, M. Bagnardi, Eruption at basaltic calderas forecast by magma flow rate. *Nat. GeoSci.* **15**, 580-584 (2022).
13. F. Sigmundsson *et al.*, Unexpected large eruptions from buoyant magma bodies within viscoelastic crust. *Nat Commun* **11**, 2403 (2020).
14. S. Barsotti *et al.*, The eruption in Fagradalsfjall (2021, Iceland): how the operational monitoring and the volcanic hazard assessment contributed to its safe access. *Natural Hazards* **116**, 3063-3092 (2023).
15. F. Sigmundsson *et al.*, Fracturing and tectonic stress drives ultrarapid magma flow into dikes. *Science*, eadn2838 (2024).

16. M. Parks *et al.*, Deformation, seismicity, and monitoring response preceding and during the 2022 Fagradalsfjall eruption, Iceland. *Bulletin of Volcanology* **85**, (2023).
17. Ó. G. Flóvenz *et al.*, Cyclical geothermal unrest as a precursor to Iceland's 2021 Fagradalsfjall eruption. *Nat. GeoSci.* **15**, 397-404 (2022).
18. J. Jenkins *et al.*, Crustal Formation on a Spreading Ridge Above a Mantle Plume: Receiver Function Imaging of the Icelandic Crust. *Journal of Geophysical Research: Solid Earth* **123**, 5190-5208 (2018).
19. S. A. Halldorsson *et al.*, Rapid shifting of a deep magmatic source at Fagradalsfjall volcano, Iceland. *Nature* **609**, 529-534 (2022).
20. K. Sæmundsson, M. Á. Sigurgeirsson, G. Ó. Friðleifsson, Geology and structure of the Reykjanes volcanic system, Iceland. *Journal of Volcanology and Geothermal Research* **391**, (2020).
21. F. Sigmundsson *et al.*, Deformation and seismicity decline before the 2021 Fagradalsfjall eruption. *Nature* **609**, 523-528 (2022).
22. G. B. M. Pedersen *et al.*, Volume, Effusion Rate, and Lava Transport During the 2021 Fagradalsfjall Eruption: Results From Near Real-Time Photogrammetric Monitoring. *Geophysical Research Letters* **49**, (2022).
23. A. Caracciolo *et al.*, in *EGU General Assembly 2024*. (Vienna, Austria, 2024).
24. I. N. Bindeman *et al.*, Diverse mantle components with invariant oxygen isotopes in the 2021 Fagradalsfjall eruption, Iceland. *Nat Commun* **13**, 3737 (2022).
25. J. Maclennan, Concurrent Mixing and Cooling of Melts under Iceland. *JPet* **49**, 1931-1953 (2008).
26. D. A. Neave, O. Shorttle, M. Oeser, S. Weyer, K. Kobayashi, Mantle-derived trace element variability in olivines and their melt inclusions. *EPSL* **483**, 90-104 (2018).
27. K. Sæmundsson, H. Jóhannesson, Á. Hjartason, S. G. Kristinsson, M. Á. Sigurgeirsson, "Geological Map of Southwest Iceland, 1:100 000," (Iceland GeoSurvey, 2010).
28. Supplementary text is available in the supplementary materials.
29. D. A. Neave, K. D. Putirka, A new clinopyroxene-liquid barometer, and implications for magma storage pressures under Icelandic rift zones. *American Mineralogist* **102**, 777-794 (2017).
30. H.-J. Yang, R. J. Kinzler, T. L. Grove, Experiments and models of anhydrous, basaltic olivine-plagioclase-augite saturated melts from 0.001 to 10 kbar. *CMP* **124**, 1-18 (1996).
31. J. Maclennan, D. McKenzie, K. Gronvöld, L. Slater, Crustal accretion under northern Iceland. *EPSL* **191**, 295-310 (2001).
32. D. W. Peate *et al.*, Historic magmatism on the Reykjanes Peninsula, Iceland: a snap-shot of melt generation at a ridge segment. *CMP* **157**, 359-382 (2009).
33. J. E. Martins *et al.*, 3D S-wave velocity imaging of Reykjanes Peninsula high-enthalpy geothermal fields with ambient-noise tomography. *Journal of Volcanology and Geothermal Research* **391**, (2020).
34. T. Greenfield *et al.*, Deep long period seismicity preceding and during the 2021 Fagradalsfjall eruption, Iceland. *Bulletin of Volcanology* **84**, (2022).
35. D. A. Neave, O. Namur, O. Shorttle, F. Holtz, Magmatic evolution biases basaltic records of mantle chemistry towards melts from recycled sources. *EPSL* **520**, 199-211 (2019).
36. H. E. Huppert, R. S. J. Sparks, J. A. Whitehead, M. A. Hallworth, Replenishment of magma chambers by light inputs. *Journal of Geophysical Research: Solid Earth* **91**, 6113-6122 (1986).

37. J. Maclennan, Mafic tiers and transient mushes: evidence from Iceland. *Phil. Trans.* **377**, 20180021 (2019).
38. F. Faure, G. Trolliard, C. Nicollet, J.-M. Montel, A developmental model of olivine morphology as a function of the cooling rate and the degree of undercooling. *CMP* **145**, 251-263 (2003).
39. J. Tarasewicz, R. S. White, A. W. Woods, B. Brandsdóttir, M. T. Gudmundsson, Magma mobilization by downward-propagating decompression of the Eyjafjallajökull volcanic plumbing system. *Geophysical Research Letters* **39**, (2012).
40. J. Maclennan, D. McKenzie, F. Hilton, K. Gronvöld, N. Shimizu, Geochemical variability in a single flow from northern Iceland. *Journal of Geophysical Research: Solid Earth* **108**, ECV 4-1-ECV 4-21 (2003).
41. A. J. Pietruszka, D. E. Heaton, J. P. Marske, M. O. Garcia, Two magma bodies beneath the summit of Kīlauea Volcano unveiled by isotopically distinct melt deliveries from the mantle. *EPSL* **413**, 90-100 (2015).
42. E. C. Bergmanis, J. Sinton, K. H. Rubin, Recent eruptive history and magma reservoir dynamics on the southern East Pacific Rise at 17°30′S. *G3* **8**, n/a-n/a (2007).
43. J. Sinton *et al.*, Volcanic eruptions on mid-ocean ridges: New evidence from the superfast spreading East Pacific Rise, 17°–19°S. *Journal of Geophysical Research: Solid Earth* **107**, (2002).
44. K. H. Rubin, J. M. Sinton, J. Maclennan, E. Hellebrand, Magmatic filtering of mantle compositions at mid-ocean-ridge volcanoes. *Nat. GeoSci.* **2**, 321-328 (2009).
45. C. Gansecki *et al.*, The tangled tale of Kilauea's 2018 eruption as told by geochemical monitoring. *Science* **366**, (2019).
46. O. Sigmarsson *et al.*, Remobilization of silicic intrusion by mafic magmas during the 2010 Eyjafjallajökull eruption. *Solid Earth* **2**, 271-281 (2011).
47. B. V. Alloway, N. J. Pearce, G. Villarosa, V. Outes, P. I. Moreno, Multiple melt bodies fed the AD 2011 eruption of Puyehue-Cordon Caulle, Chile. *Sci Rep* **5**, 17589 (2015).
48. O. Sigmarsson, M. Condomines, S. Fourcade, A detailed Th, Sr and O isotope study of Hekla: differentiation processes in an Icelandic Volcano. *CMP* **112**, 20-34 (1992).
49. E. Martin, O. Sigmarsson, Crustal thermal state and origin of silicic magma in Iceland: the case of Torfajökull, Ljósufjöll and Snæfellsjökull volcanoes. *CMP* **153**, 593-605 (2007).
50. P. Wieser *et al.*, Thermobar: An open-source Python3 tool for thermobarometry and hygrometry. *Volcanica* **5**, 349-384 (2022).
51. F. A. Darbyshire, R. S. White, K. F. Priestley, Structure of the crust and uppermost mantle of Iceland from a combined seismic and gravity study. *EPSL* **181**, 409-428 (2000).
52. A. Caracciolo *et al.*, Medieval and recent SO2 budgets in the Reykjanes Peninsula: implication for future hazard. *GPL* **30**, 20-27 (2024).
53. J. T. Armstrong, in *Electron probe quantitation*. (Springer, 1991), pp. 261-315.
54. E. Jarosewich, Smithsonian microbeam standards. *Journal of research of the National Institute of Standards and Technology* **107**, 681 (2002).
55. K. P. Jochum *et al.*, GeoReM: A New Geochemical Database for Reference Materials and Isotopic Standards. *Geostandards and Geoanalytical Research* **29**, 333-338 (2005).
56. C. Pin, A. Gannoun, A. Dupont, Rapid, simultaneous separation of Sr, Pb, and Nd by extraction chromatography prior to isotope ratios determination by TIMS and MC-ICP-MS. *J. Anal. At. Spectrom.* **29**, 1858-1870 (2014).

57. R. J. M. Baxter, J. Maclennan, Influence of magma flux on magma storage depths along the Reykjanes Ridge. *EPSL* **631**, (2024).
58. E. Bali, M. E. Hartley, S. A. Halldórsson, G. H. Gudfinnsson, S. Jakobsson, Melt inclusion constraints on volatile systematics and degassing history of the 2014–2015 Holuhraun eruption, Iceland. *CMP* **173**, (2018).
59. A. MacDonald, T. Ubide, S. Mollo, A. Pontesilli, M. Masotta, The Influence of Undercooling and Sector Zoning on Clinopyroxene–Melt Equilibrium and Thermobarometry. *JPet* **64**, (2023).
60. K. D. Putirka, Thermometers and Barometers for Volcanic Systems. *Reviews in Mineralogy and Geochemistry* **69**, 61-120 (2008).
61. A. R. L. Nichols, M. R. Carroll, Á. Höskuldsson, Is the Iceland hot spot also wet? Evidence from the water contents of undegassed submarine and subglacial pillow basalts. *EPSL* **202**, 77-87 (2002).
62. D. Tian *et al.*, PyGMT: A Python interface for the Generic Mapping Tools (2024); https://doi.org/ 10.5281/zenodo.10578540.
63. P. Wessel *et al.*, The Generic Mapping Tools Version 6. *G3* **20**, 5556-5564 (2019).
64. J. D. Hunter, Matplotlib: A 2D graphics environment. *Computing in Science & Engineering* **9**, 90-95 (2007).
65. The pandas development team, pandas-dev/pandas:Pandas (2020); https://doi.org/ 10.5281/zenodo.3509134.
66. W. McKinney, in *Proceedings of the 9th Python in Science Conference*. (2010), pp. 56-61.
67. C. R. Harris *et al.*, Array programming with NumPy. *Nature* **585**, 357-362 (2020).
68. R. W. Le Maitre *et al.*, *Igneous rocks: a classification and glossary of terms: recommendations of the International Union of Geological Sciences Subcommission on the Systematics of Igneous Rocks*. (Cambridge University Press, 2005).
69. B. J. Wood, J. D. Blundy, A predictive model for rare earth element partitioning between clinopyroxene and anhydrous silicate melt. *CMP* **129**, 166-181 (1997).
70. O. Namur, B. Charlier, M. J. Toplis, J. Vander Auwera, Prediction of plagioclase-melt equilibria in anhydrous silicate melts at 1-atm. *CMP* **163**, 133-150 (2011).
71. H. Palme, H. S. C. O'Neill, in *Treatise on Geochemistry*. (2014), pp. 1-39.

Acknowledgments: We gratefully acknowledge help with sample collection by Cèline Mandon, Elisa Piispa, and Robert Askew. Freysteinn Sigmundsson, Halldór Geirsson, and John Maclennan are thanked for helpful discussions. Constructive reviews by Adam Kent, Teresa Ubide, and an anonymous reviewer helped improve the manuscript. The geographic information provided by the National Land Survey of Iceland was extremely valuable for constraining the relative timing of lava emplacement and planning the field sampling campaigns. The photographs of the earliest phases of the December 2023 eruption made publicly available by Björn Oddson at the Department of Civil Protection and Emergency Management and made publicly available played an important role in identifying the sequence of lava flow emplacement. We also acknowledge the GPS data made publicly available by the University of Iceland and the Icelandic Meteorological Office.

Funding:

Icelandic Research Fund Grant of Excellence 228933-053 (EB, SAH)
Icelandic Research Fund Grant 206755-052 (GBMP)

Author contributions:

Conceptualization: SWM, AC, EB, SAH, OS, GHG

Methodology: SWM, AC, EB, SAH, OS, GHG, GBMP, JGR, EWM, VD

Investigation: SWM, AC, EB, SAH, OS, GHG, GBMP, JGR, AAA, BYG, CB, DA, HM, NL, NL, RHR, SMJ, SS, VD.

Visualization: SWM

Funding acquisition: EB, SAH

Project administration: EB, SAH, OS

Writing – original draft: SWM

Writing – review & editing: SWM, AC, EB, SAH, OS, GHG, GBMP, JGR, EWM, AAA, BYG, HM, NL, NL, RHR, SMJ, SS, VD.

Competing interests: Authors declare that they have no competing interests.

Data and materials availability: All data are available in the main text or the supplementary materials.

Supplementary Materials

Materials and Methods

Supplementary Text

Figs. S1 to S24

Tables S1 to S7

References (*49-67*)

Data S1 to S5

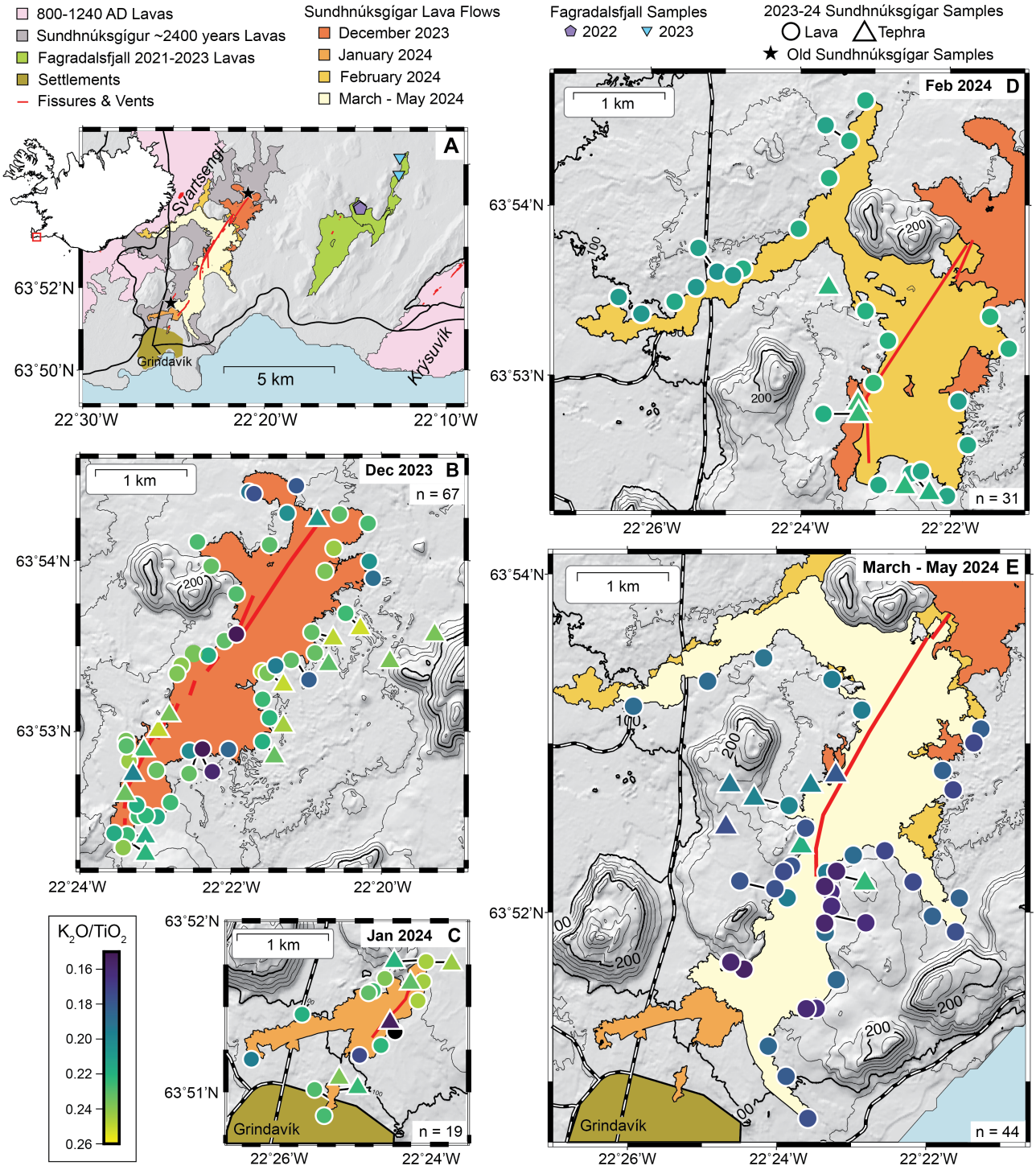

Fig. 1. The locations of the lava flows, fissures, and where lava and tephra samples were collected. (A) The locations of the recent lava flows, lava flows emplaced in the 800-1240 AD fires, and the extent of the lava last erupted at Sundhnúksgígar (~2400 years ago). Italic text indicates the Svartsengi, and Krýsuvík volcanic systems. Sampling locations for the 2400 year old Sundhnúksgígar tephra and the 2022 and 2023 Fagradalsfjall material are indicated. The inset shows the location of the map area within Iceland. **(B)** The locations from which samples were collected from the December 2023 lava and tephra. The shading indicates the whole rock K_2O/TiO_2. **(C)** The same for the January 2024 eruption. **(D)** The same for the

February 2024 eruption. **(E)** The same for the March-May 2024 eruption. The number of samples collected from each eruption are given in the corner of (B), (C), (D), and €. The geological data are provided by the Iceland GeoSurvey (ÍSOR) (*27*), and the geographic data are provided by the National Land Survey of Iceland.

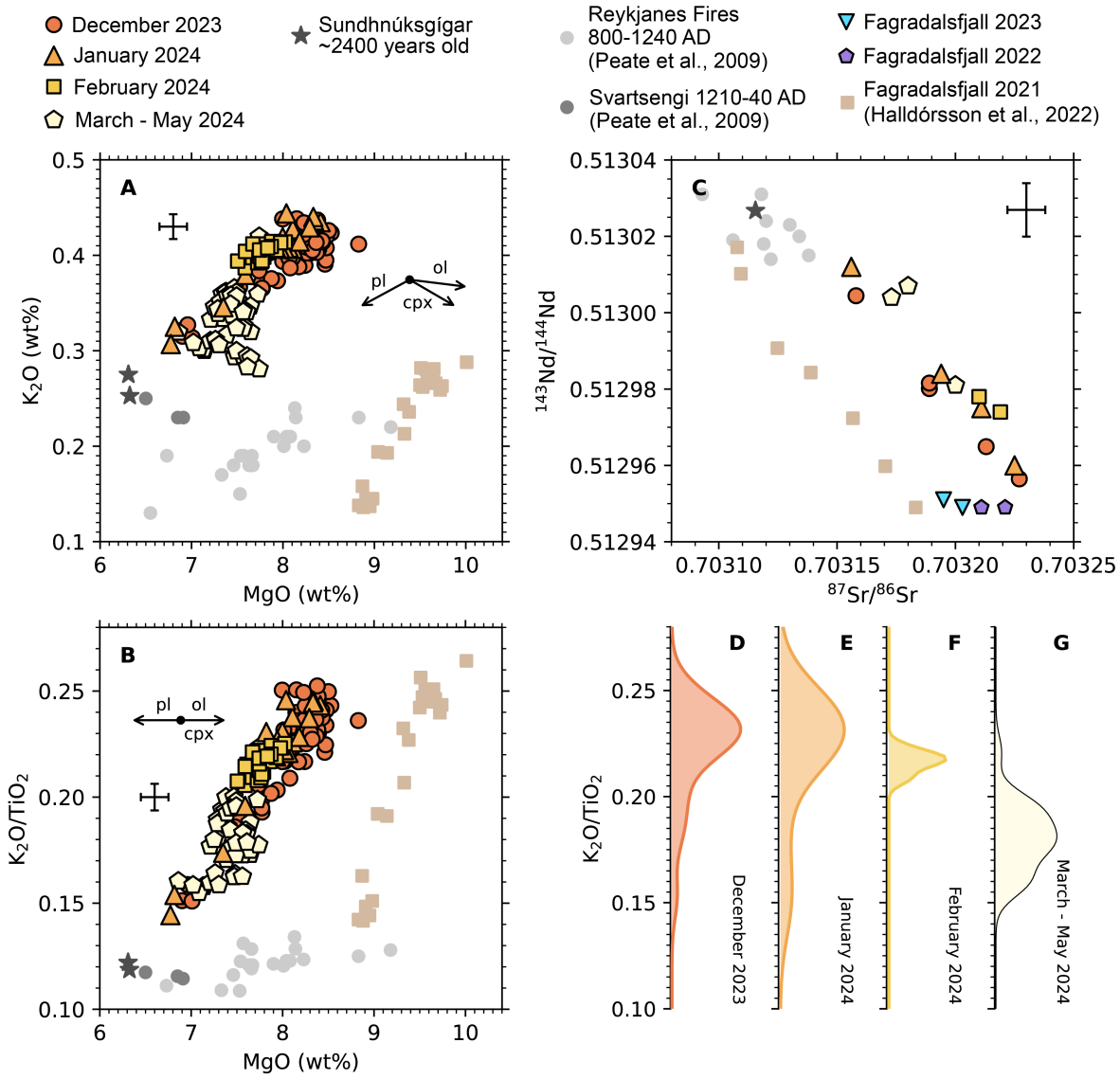

Fig. 2. Comparison of the geochemical variations in the erupted lava and tephra with other Reykjanes lavas. (A) Whole rock K_2O and MgO concentrations. **(B)** Whole rock K_2O/TiO_2 ratios vs MgO concentrations. The vectors in (A) and (B) show the effects of olivine (ol), clinopyroxene (cpx), and plagioclase (pl) accumulation on the whole rock composition. Crystal fractionation will result in the opposite sense of change. The error bars in (A) and (B) show representative 2σ on repeated standard analyses across all measurement sessions. The accuracy of the analyses was within this range. **(C)** Sr and Nd radiogenic isotope ratios from whole rocks and glasses. The error bars show the maximum values of 2 s.e. (standard error) precision; analyses of rock standards reproduced accepted values within this range. **(D, E, F, G)** show kernel density estimates of the K_2O/TiO_2 ratios of the material sampled in each eruption. The horizontal lines show the mean composition of the samples from each eruption and the 2 s.e. of the estimate. The Fagradalsfjall 2021 data is from (*19*) and the data from historical Reykjanes is from (*32*).

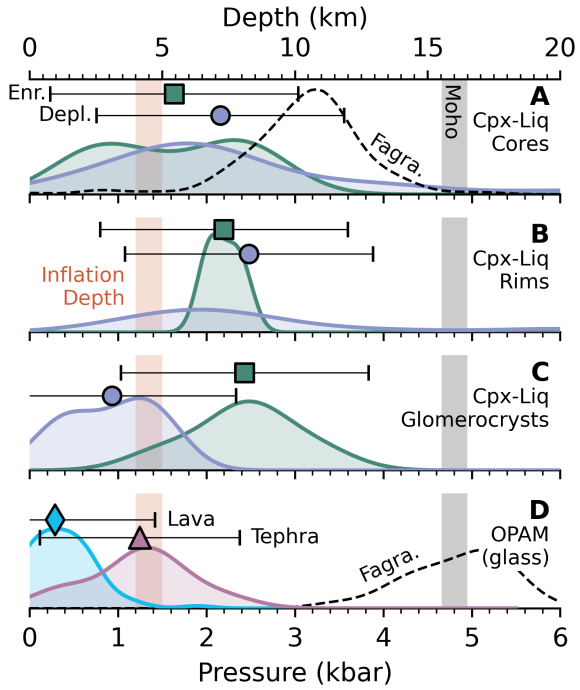

Fig. 3. Magma equilibration pressures derived from OPAM and clinopyroxene-liquid barometry. (A) shows the clinopyroxene-liquid (*29, 50*) equilibration pressures calculated from crystal core compositions in depleted ($K_2O/TiO_2 < 0.19$) and enriched ($K_2O/TiO_2 > 0.19$) whole rocks. The dashed line shows the clinopyroxene-liquid pressures reported by (*19*) for Fagradalsfjall clinopyroxene crystal cores. **(B)** and **(C)** show the same for rims and glomerocrysts. **(D)** shows the OPAM (*1, 10, 30*) equilibration pressures for glass analyses where the probability of fit is 0.8 or greater. The dashed line shows the OPAM pressures obtained by (*19*) for tephra from Fagradalsfjall. In all panels the symbols show the mean pressure estimate and the error bars the standard error of the estimate (*1, 29*). The depth scale is calculated assuming the density of the crust is 3000 kg m^{-3} (*1, 51*). A Moho depth appropriate for the Reykjanes peninsula is indicated (*18*). The range of depths modelled for the inflation source (*15*) is shown by the shaded band at 4-5 km.

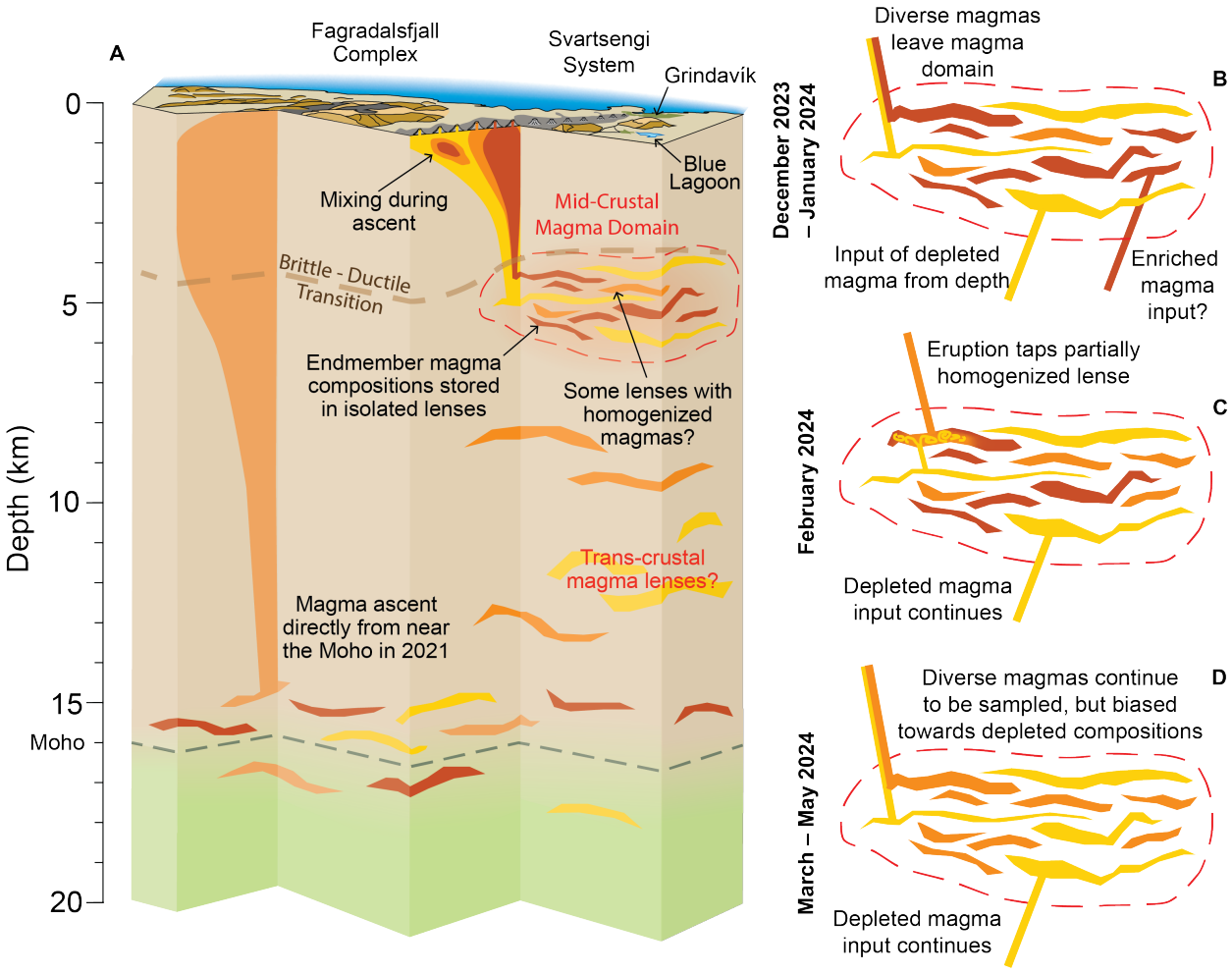

Fig. 4. The structure of the mid-crustal magma domain beneath Svartsengi and its evolution with time. (A) Schematic overview of the crustal magmatic system beneath Fagradalsfjall and Svartsengi. The diagram is drawn looking towards the Southeast. Enriched magmas are indicated by darker shading (red) than the depleted magmas (yellow). The magma domain is indicated at ~4~6 km depth based on the overlap between the clinopyroxene-liquid and OPAM barometers (Fig. 2), as well as the modelled inflation depth (*15, 17*). The brittle-ductile transition is indicated at a depth similar to that suggested by (*15*). **(B, C, D)** Schematic evolution of the magma domain throughout the eruptions.

Science
AAAS

Supplementary Materials for

A dynamic mid-crustal magma domain revealed by the 2023-24 Sundhnúksgígar eruptions, Iceland

Simon W. Matthews[1]*, Alberto Caracciolo[1], Enikő Bali[1], Sæmundur A. Halldórsson[1], Olgeir Sigmarsson[1,2], Guðmundur H. Guðfinnsson[1], Gro B. M. Pedersen[1,3], Jóhann Gunnarsson Robin[1], Edward W. Marshall[1,4], Araksan A. Aden[1], Bryndís Ýr Gísladóttir[1], Chantal Bosq[2], Delphine Auclair[2], Heini Merrill[1], Nicolas Levillayer[1], Noëmi Löw[1], Rebekka Hlín Rúnarsdóttir[1], Sóley M. Johnson[1], Sveinbjörn Steinþórsson[1], Vincent Drouin[3]
Corresponding author: simonm@hi.is

The PDF file includes:

Other Supplementary Materials for this manuscript include the following:

Materials and Methods

Sample collection

A small number of samples were collected during eruption, from recently solidified lava, recently fallen tephra, or by direct sampling of flowing lava followed by quenching in water. More extensive sampling campaigns were completed following the end of the eruption where we aimed to collect samples representing lava and tephra erupted from different parts of the fissure at different times throughout the eruption. Where possible, glassy crusts were collected in favor of the solidified middle of the lava flows. Dataset S1 includes GPS sample locations as well as brief descriptions of the unit sampled. Following sample collection, the material was catalogued and dried. The samples are currently housed at the Institute of Earth Sciences, University of Iceland, but will be deposited with the Institute of Natural History, Iceland. A total of 66 samples were collected from the December eruption, 18 samples from the January eruption, 30 from the February eruption and 44 from the March-May eruption. In addition, two samples (Sund-01 and SHA) were collected from the old Sundhnúksgígar craters, erupted ~2400 years ago.

ICP-OES whole rock major element analysis

Representative portions of the samples were powdered using a shatterbox with a tungsten carbide grinding container. The container was cleaned with water and compressed air between samples and was pre-contaminated by powdering a smaller amount of sample material. A mixture of 100 mg of sample powder and 250 mg of $LiBO_2$ were fluxed at 1000˚C in a graphite crucible for ~40 minutes. The cooled glass bead was then dissolved in 50 ml 5% nitric acid. Solutions of USGS standards BHVO-1, BIR-1 and W-2, in addition to in-house reference materials A-THO, B-THO, B-ALK and MSR161014-1 were prepared the same way. The concentrations of SiO_2, Al_2O_3, FeO, MnO, MgO, CaO, Na_2O, K_2O, TiO_2, and P_2O_5 were then determined by inductively coupled plasma optical emission spectroscopy (ICP-OES) using the ThermoFisher iCAP 7400 Duo instrument at the University of Iceland Plasma Center. The in-house standards A-THO, B-THO and B-ALK were used to calibrate the instrument, MSR161014-1 was run every 5 samples to monitor drift and repeated analyses of BIR-1, BHVO-1, and W-2 were used to assess accuracy and precision (figs. S14, S15, Dataset S2). B from the $LiBO_2$ was used as an internal standard.

The values for 2σ reproducibility on K_2O/TiO_2 across all OES sessions for BHVO-1 and W2 are 4.6% and 5.9%, respectively (fig. S16). The reproducibility for K_2O/TiO_2 is substantially worse for BIR-1, with a 2σ value of 37%, owing to the concentration of K_2O being an order of magnitude lower. However, the material erupted in the 2023 and 2024 eruptions at Sundhnúksgígar have K_2O and TiO_2 concentrations of a similar order to BHVO-1 and W2, hence a 2σ intersession reproducibility of 5.9% is appropriate for K_2O/TiO_2 in these samples.

EPMA glass and mineral analysis

Major element compositions of groundmass glass (n=398), melt inclusion glass (n=50), plagioclase (n=67), olivine (n=91), clinopyroxene (n=168) and spinel (n=69) were determined in grain mounts by electron probe microanalysis (EPMA) using the JEOL JXA-8230 SuperProbe at the Institute of Earth Sciences, University of Iceland. In addition, glass analyses from three samples (G20231220-1, G20240114-4, and G20240208-2) and 39 melt inclusions acquired in the same analytical sessions, but published by (*52*), are included in the compilation and figures. To address the lack of glass in the depleted material erupted in December, analyses (n=6) were obtained from the microcrystalline matrix of G20231221-3

using a defocused beam, along with glass hosted in embayments, with the aim of constraining the matrix K_2O/TiO_2 ratio for comparison with the whole rock (S4).

The microprobe is equipped with five wavelength-dispersive spectrometers (WDS) and an energy-dispersive spectrometer. Analyses were acquired using a 15 keV accelerating voltage and a probe current of 10 nA for glass and plagioclase analyses, and 20 nA for olivine, spinel, and clinopyroxene analyses. Groundmass glasses were analyzed with a defocused electron beam of 10 µm. To avoid Na loss in glasses, Na was always analyzed first on its spectrometer with a relatively short counting time (20 s on the peak, 10 s on the background). For all other elements, counting times were 30-40 s on the peak and 15-20 s on the background. All mineral phases were analyzed with a beam size of 5 µm. Counting times for olivine and clinopyroxene analyses were 30 s on peak and 15-30 s on background, while for plagioclase crystals the counting times were 40 s and 20-40 s on peak and background, respectively. The CITZAF correction program (*53*) was used for all analyses. Information on the standardization and counting times are given in Tables S1-S5.

Precision and accuracy were estimated by repeat measurements on secondary standard materials at the start and end of each session and are reported in Data S3. The accuracy of the K_2O/TiO_2 ratio measured in the glass was within the precision (2σ) of 5.5%. For most oxides measured in the glass standard, the session means are within 2 standard deviations of the accepted values (*54*) (fig. S17). For the other oxides they are within the range of values reported on GEOREM (*55*). The accuracy and precision on olivine Fo, clinopyroxene Mg#, spinel Mg#, and plagioclase An are all better than 2%. The full dataset is provided in Data S3.

ICP-MS trace element analysis

For each sample ~50 mg of cleaned and picked glass was digested in a mixture of distilled HF-HNO_3 in acid-cleaned Savillex Teflon beakers in the metal-free clean laboratory at the University of Iceland Plasma Center. Residual fluorides were removed by repeated reflux in 6M HCl acid until they could no longer be seen. They were then brought up in 6M HCl acid, before being further diluted in a 2% HNO_3 and 1% HCl solution (dilution factor of ~5000), acidified to about 0.05% HF and spiked with an In-Re solution, used as an internal standard. The samples were then transferred into acid-leached vials. Trace element concentrations were determined on the ThermoFisher iCAP RQ Quadrupole Inductively Coupled Plasma Mass-Spectrometer (ICP-MS) at the University of Iceland Plasma Centre, using a HF resistant inlet system. Powders of BIR-1, BCR-2, AGV-2, and W-2 standards were prepared in the same way and used for calibration. A solution of the BHVO-2 standard powder (also prepared in the same way) was used to assess accuracy. Most elements were within 1% of the GEOREM (*55*) preferred values (Dataset S4), including La, Yb, Ce, and Y, which are used in fig. S5.

Sr and Nd radiogenic isotope analysis

Sr and Nd isotopes were analyzed at Laboratoire Magmas et Volcans at Université Clermont Auvergne using a Triton (ThermoScientific) thermal ionization mass spectrometer. Tephra and lava samples were crushed in a jaw crusher and powdered in an agate bowl using a planetary mill. A separate aliquot of crushed SHA was leached in ~1M HCl in an ultra-sonic batch for 30 minutes, with the leachate reserved and put through the following chemistry. The leached sample was then powdered. Approximately 100 mg of powder was dissolved in concentrated HF and HNO_3 acids in a 3:1 ratio, and the fluoride residue was reduced by repeated dissolution and evaporation in 6N HCl and 14N HNO_3. Isolation of Sr and Nd followed the protocol from (*56*), and their isotope ratios were measured by thermal ionization mass spectrometry. Strontium isotope ratios were normalized to $^{86}Sr/^{88}Sr = 0.1194$

and to the recommended value of the NIST 987 standard ($^{87}Sr/^{86}Sr = 0.710245$). International reference materials were used to ensure accuracy and precision, as described in (19). The data is reported in Data S5.

OPAM Geothermobarometry

Calculations were performed using the pyOPAM script (1,*57*) which implements the parameterization by (29) and the filtering procedure of (*57*). Following (1,*57*), we exclude results that have a probability of fit < 0.8. Though this is an arbitrary cut off, fig. S18 shows that this does not bias the predicted pressures. Where analyses have a probability of fit > 0.8, other analyses from the same sample do not, which is likely caused by small scale compositional heterogeneity caused by partial re-equilibration during ascent or eruption (fig. S18B). Most of the tephra erupted contains microlites (fig. S2C,D), likely formed during ascent and eruption, and this provides an explanation for why most of the tephra samples do not have any analyses which pass the equilibrium criteria. The uncertainties in the electron probe analyses are not directly propagated but are indicated by the scatter in pressure estimates (fig. S11). When converting pressures to depth, a density of 3000 kg m^{-3} is assumed for the crust (1,50). The results from applying the OPAM barometer (including the probability of three phase saturation) are given in Data S3.

Clinopyroxene-liquid barometry

Equilibration pressures for clinopyroxene and liquid were estimated using the cpx-liquid barometer (29). Calculations were performed with the ThermoBar python library (50). Equilibrium was tested between glass analyses (from all three eruptions) and clinopyroxene core, rim, and glomerocryst analyses. The criteria used for identifying equilibrium were those recommended by (*59*). Analyses with a jadeite component of < 0.01 were removed, following the recommendation of (29), due to their proximity to the detection limit for Na. This removed a small number of points with negative calculated pressures (fig. S19C). The clinopyroxene analyses from depleted (low K_2O/TiO_2) whole rocks match with both depleted and enriched glass compositions (figs. S20-S22), but the pressure dependance of this is weak and well within the uncertainty of the barometer (±1.4 kbar). Though the majority of the estimated equilibration pressures cluster around 1-3 kbar, a small number of clinopyroxene-liquid pairs (from three clinopyroxene crystals, all from the same sample) return pressures up to ~6 kbar, with the highest two pressures associated with analyses of clinopyroxene rims (fig. S23). These higher-pressure estimates are associated with a higher jadeite component in the clinopyroxene (Fig. S19C) and may represent locally higher Na_2O contents surround the growing clinopyroxene crystals. The uncertainty in the electron probe analyses is not directly propagated, but is indicated by the scatter in mean pressures estimates (fig. S23). When converting pressures to depth, a density of 3000 kg m^{-3} is assumed for the crust (1,51). The results of the clinopyroxene-liquid barometry are given in Data S3.

Liquidus temperature calculations

For estimating the liquidus temperatures two thermometers are used. The first is Eqn. 15 from (*60*) which is calibrated on experimental olivine-saturated liquids incorporating terms for the pressure, liquid Mg#, and MgO, FeO, Na_2O, K_2O and H_2O concentrations. The H_2O concentration for each sample was estimated using the correlation observed between K_2O and H_2O in minimally degassed Icelandic glasses (*61*), by scaling linearly between 0.45 wt% H_2O for 0.3 wt% K_2O and 0.8 wt% H_2O for 0.6 wt% K_2O. The uncertainty in the temperatures derived from this equation is ±46˚C (49). The second thermometer is Eqn. 16 from (*60*) which is calibrated on experimental liquids saturated in olivine, plagioclase, and clinopyroxene. The calibration incorporates terms for pressure, and mole fractions of SiO_2,

Al_2O_3, MgO, SiO_2, and Al_2O_3 in the liquid. Temperatures estimated using this thermometer have an uncertainty of ±19˚C (50). For both thermometers a pressure of 2 kbar was used, consistent with the results from clinopyroxene-liquid barometry. Calculations were performed using the ThermoBar python library (50). The results are tabulated in Data S3 and are shown in fig. S12.

Identifying the timing of lava emplacement

A small number of the lava samples were collected from active flow fronts, meaning the timing of flow emplacement is defined precisely. For samples collected from cooled flows we estimated the timing of their emplacement by comparing the GPS coordinates of the sampling location with remote sensing data (made publicly available by the National Land Survey of Iceland) using the geographic information system software QGIS.

18-21 December 2023 eruption: Online web camera data provided the times that particular segments of the fissure opened and then became inactive. Due to the bad weather during most of the eruption, the first map of the lava flow field was produced at the very end of the eruption on December 21st, based on orthomosaics and lava thickness maps from an aerial survey that day. At that time only one part of the lava field was active. Most of the lava field was emplaced during the night between December 18th 22:17 and December 19th 06:00. During this period two helicopter flights (December 18th 23:30- December 19th 00:30, and December 19th 04:30-05:30) were made to the area. On these flights, oblique photographs were taken covering the whole area, providing constraints on which lobes were active during these times. In addition, four ICEYE SAR amplitude images were acquired on December 19th at 03:57, 11:34, 17:49, and on December 21st at 03:03, with variable inclination angles and resolutions. However, identification of the lava flow fronts on the eastern side of the area was difficult due to the similarity in roughness between the new lava and pre-existing lava field.

14-16 January 2024 eruption: Online web camera data provide information on the timing of the opening of the two fissures, and when the activity had shut down. Four aerial acquisitions providing orthomosaics, lava flow thickness maps, and lava outlines were used to identify the approximate timing of activity in the lava field at the lava sample locations. The aerial acquisitions were obtained on January 14 at ~13:50; ~14:00 and ~17:00 and Jan. 15 at ~14:00.

8-9 February 2024 eruption: Online web camera data provide information on the timing of the opening of the fissures, the progression of the western lava flow that crossed the road Grindavíkurvegur and the hot water pipes, and the time when activity had ceased. Two flights providing orthomosaics, lava flow thickness maps and lava outlines were acquired on February 8 at ~13:00 and ~17:00 and another flight were acquired on February 14 after the eruption had stopped.

March 16th-May 2024 eruption: The time range of lava emplacement was determined from a combination of webcam and field observations, with coarser time constraints than the previous eruptions.

Where it was possible to constrain the timing of lava and tephra emplacement, this is given in Data S1. A qualitative assessment of the confidence in the time constraints is given, determined by the clarity of the remote sensing data and photo observations.

Software used for preparing figures and for data analysis

Figures were prepared using pyGMT (*62, 63*) and Matplotlib (*64*). Data analysis was performed using pandas (*65, 66*) and numpy (*67*). Other software is cited in the appropriate methods section above.

Supplementary Text

Temporal patterns in the geochemical variability.

Though the constraints on the relative timing of tephra deposition and lava emplacement during the December eruption remains largely uncertain (Fig. S7A), some qualitative constraints can be placed on the relative timing. The tephra deposited far from the vents (at the far east of the area shown in Fig. 1B and adjacent to the eastern lava front) is enriched. Where the tephra was collected adjacent to the lava flows, no tephra was seen on top of the lava, indicating it was deposited early and likely during the intense fountaining at the start of the eruption. The last major lobe to be emplaced at the edge of the flow field was at the northwestern extent, which consisted of depleted lavas (Fig. 1A, fig. S9C). The tephra samples collected from close to the vents at the southern and northern extremities of the fissure show some variability in their ratios (Fig. 1B). These vents were active only near the start of the eruption yet display moderately low to high K_2O/TiO_2 ratios. As the eruption continued, lavas were largely emplaced on top of the flows emplaced within the first hours of the eruption. Samples could not be obtained from the middle of the lava field for safety reasons.

In the March-May 2024 eruption, lavas emplaced after the resumption of inflation in early April have a slightly higher K_2O/TiO_2 ratio than those emplaced immediately before (fig. S7D), though it is unclear if there is a causative link.

Spatial patterns in the geochemical variability

While the composition of erupted lava displays some systematic behavior with time, we might expect a spatial control on the composition of erupted material also. For example, different parts of the fissure were more and less active at different times (i.e., during fissure opening and then concentration of activity onto a small number of vents), so if there was a systematic difference in the composition of the material erupted from each vent, this could propagate into temporal variability. In the December 2023 lava field there is some evidence to suggest there is some spatial control on the variability; where depleted lavas are seen on one side of the fissure, there are depleted lavas nearby on the opposite side (Fig. 1B). This is most clearly seen in the northernmost part of the lava field, where a depleted lobe is seen on the western side of the fissure, and to the southeast (across the fissure) there were two relatively depleted samples analyzed also. The emplacement of the northernmost part was caught on camera around 04:30-05:30 (fig. S24B). While the northernmost part of the fissure is still active, it appears to be feeding lava to the northeast (which is relatively enriched), instead the northernmost lobe is fed from the fissure segment slightly further south. The depleted samples on the opposite (eastern) side of the fissure flow seem to have been emplaced before the image was taken. It is plausible they were fed from the same part of the fissure (fig. S24B).

The southernmost depleted samples (Fig. 1B) occur in close proximity to more enriched lavas (Fig. S24C). However, these changes occur across contacts between different flow units, identifiable in the field (Fig. S24D). It is difficult to assign these units to different parts of the fissure, particularly because later emplaced lavas remove evidence of the emplacement of earlier lavas. Much of this complexity is seen on the eastern side of the lava field, but the webcams monitoring the area were all located on the western side. However, it is plausible that this small scale variability in composition recorded at the edges of the lava field is due to the complex emplacement of the lavas, where the direction of lava flow from particular vents is ever changing, particularly early on in the eruption when effusion rates were high.

Crystallinity of the samples

The data reported here do not allow for accurate estimates of the fraction of macrocrysts in the samples. However, approximate crystallinities can be obtained by assuming the composition of the glass is related to the composition of the whole rock by adding the crystal cargo. Fig. S25 shows the results of this analysis using K_2O, and assuming K_2O is not incorporated into the crystal cargo in significant quantities. The mean value of the estimated crystallinity (by mass) is 15% and the standard deviation is 9%. This is consistent with qualitative observations of the hand specimens. No significant differences are seen between the eruptions.

Mixing endmembers

To investigate the relationship between the depleted and enriched endmembers seen in the Sundhnúksgígar products and the Fagradalsfjall 2021 products (19), some illustrative mixing models were developed. We consider the $^{87}Sr/^{86}Sr$-$^{143}Nd/^{144}Nd$ systematics first, and then separately K_2O/TiO_2-La/Yb. We then show that while models can be developed in both spaces that match the data, they are inconsistent with each other, ruling out either endmember composition being the same in the Sunhnúksgígar magmas and the Fagradalsfjall magmas.

Since mixing arrays in $^{87}Sr/^{86}Sr$-$^{143}Nd/^{144}Nd$ space are curved, when considering only this space (and no other chemical parameters) it would be possible to find two mixing lines from identical depleted and enriched endmembers that can match both Sundhnúksgígar and Fagradalsfjall. However, the curvature depends on the relative Sr and Nd concentrations. The solid black lines in figs. S26 and S27A,B show the mixing model between possible endmembers identified for the Sundhnúksgígar products. The grey dashed line shows the mixing curve that is generated by mixing between the same endmembers but while simultaneously matching the Sr and Nd concentrations in the Fagradalsfjall 2021 lavas. The poor fit of the dashed line to the Fagradalsfjall 2021 data indicates that the mixing endmembers cannot have identical $^{87}Sr/^{86}Sr$ and $^{143}Nd/^{144}Nd$ ratios for both Sundhnúksgígar and Fagradalsfjall. It is possible, however, to find a model that matches the observations but with the same depleted endmember and different enriched endmembers (the dotted line in Figs. S26 and S27A,B). The mixing model parameters are given in Table S6.

Likewise, a model can be developed that matches the K_2O-TiO_2 and La-Yb systematics for Fagradalsfjall and Sundhnúksgígar, with a single depleted endmember and different enriched endmembers (Figs, S5C, S26, S27C,D). The mixing model parameters are given in Table S7. However, the depleted endmember must be extended to a much more extreme composition than for the Sr-Nd isotope systematics. Consequently, the mixing models that match the K_2O-TiO_2 and La-Yb systematics with a single depleted endmember require different mixing proportions (indicated by the dots at 10% increments on each model line) for each sample relative to the mixing models that match the Sr-Nd systematics. The two models are mutually inconsistent, demonstrating that both the depleted and enriched endmember have distinct compositions to those seen at Fagradalsfjall.

The extent of fractional crystallization of the endmember melts

Though the preceding section has ruled out that endmembers of the same composition are parental to both the Fagradalsfjall and Sundhnúksgígar magmas, the compositional differences are subtle. The higher concentrations of incompatible elements (e.g., K_2O, TiO_2, La, Yb) in the Sundhnúksgígar magmas (compared to Fagradalsfjall) is most likely generated largely by differing amounts of fractional crystallization, with the concentrations in the primary melts playing a subordinate role. Though the whole rock compositions are variably affected by crystal accumulation, which will act to dilute the incompatible elements, it likely has a similar magnitude effect in both the Fagradalsfjall and Sundhnúksgígar whole rocks.

The relative K_2O concentrations of the endmember magmas can therefore be used to provide an approximate estimate of the additional amount of crystallization experience by the Sundhnúksgígar magmas.

Assuming perfect incompatibility, the relative amount of fractional crystallization between a more primitive melt C_0 and evolved melt C_1 is given by:

$$X = 1 - \frac{C_0}{C_1}$$

The maximum and minimum K_2O concentrations are used for the enriched and depleted melts, respectively, with C_0 derived from the Fagradalsfjall whole rock compositions (19), and C_1 from the Sundhnúksgígar whole rock compositions. This gives 46% crystallization for the depleted endmember and 35% crystallization for the enriched endmember.

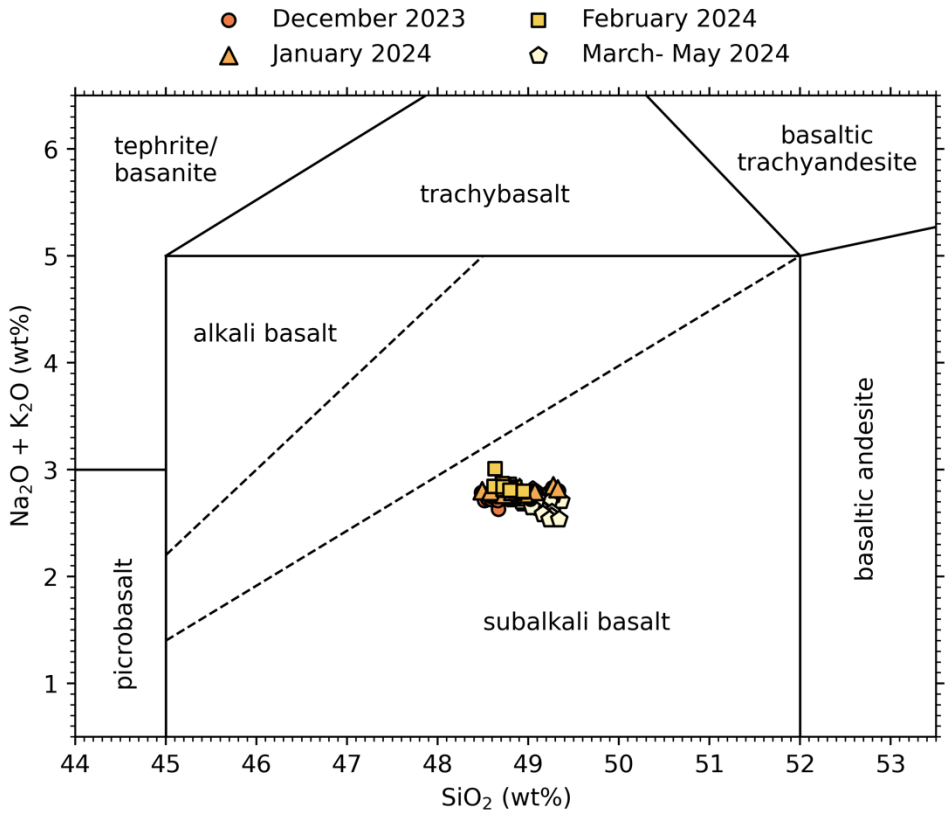

Fig. S1

Whole rock analyses from the eruptions shown on a total alkalis-silica (TAS) plot, after (*68*).

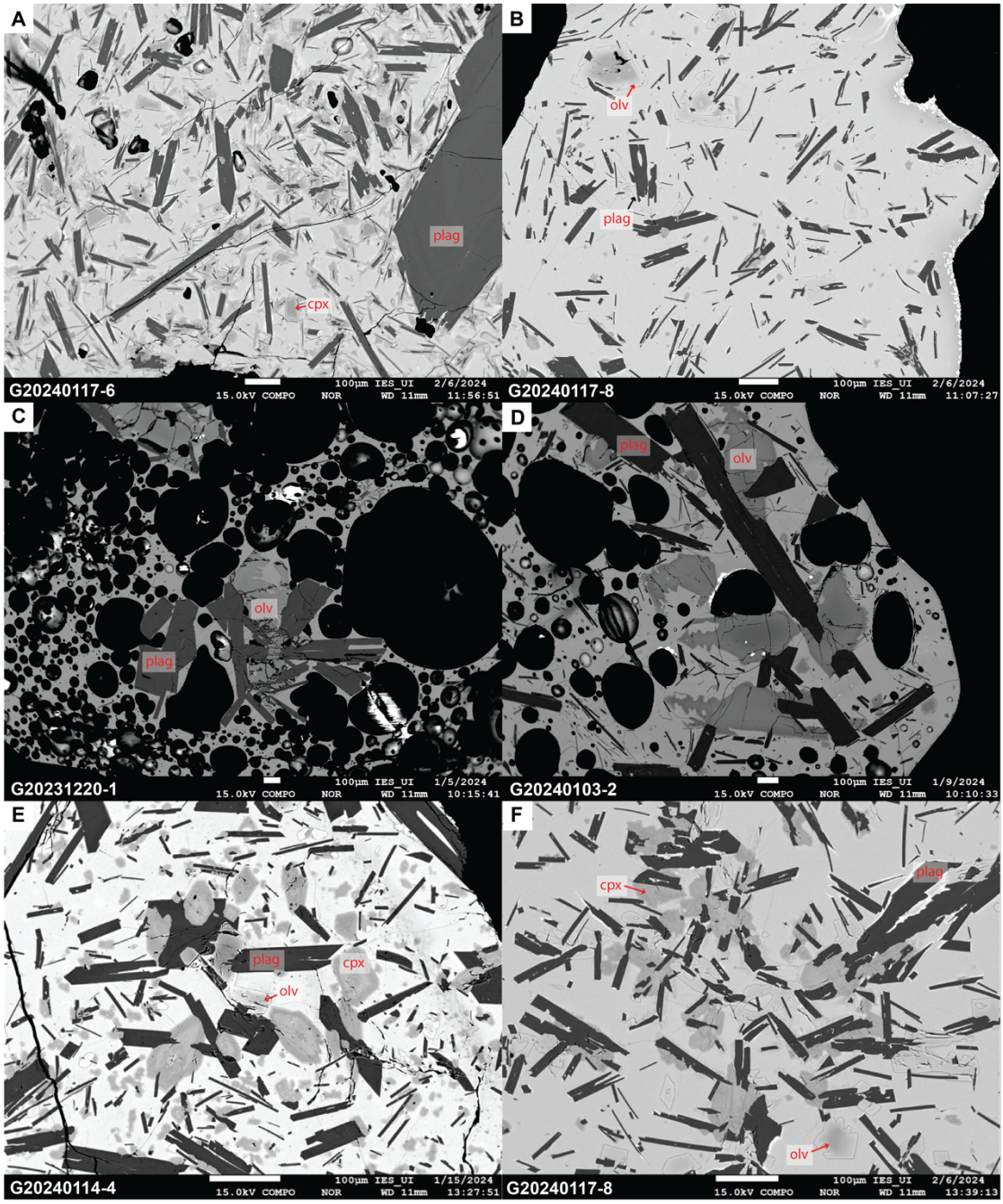

Fig. S2

Backscatter electron images showing typical textures of the Sundhnúksgígar products. (A) shows the relatively microlite-rich glassy lava G20240117-6 from the January eruption. (B) shows glassy lava crust G20240117-8 from the January eruption. (C) shows vesicle-rich tephra G20231220-1 erupted in December. (D) shows tephra G20240103-2 also erupted in December. (E) and (F) show glomerocrysts of clinopyroxene (cpx), plagioclase (plag), and olivine (olv) in lavas G20240114-4 and G20240117-8 erupted in January.

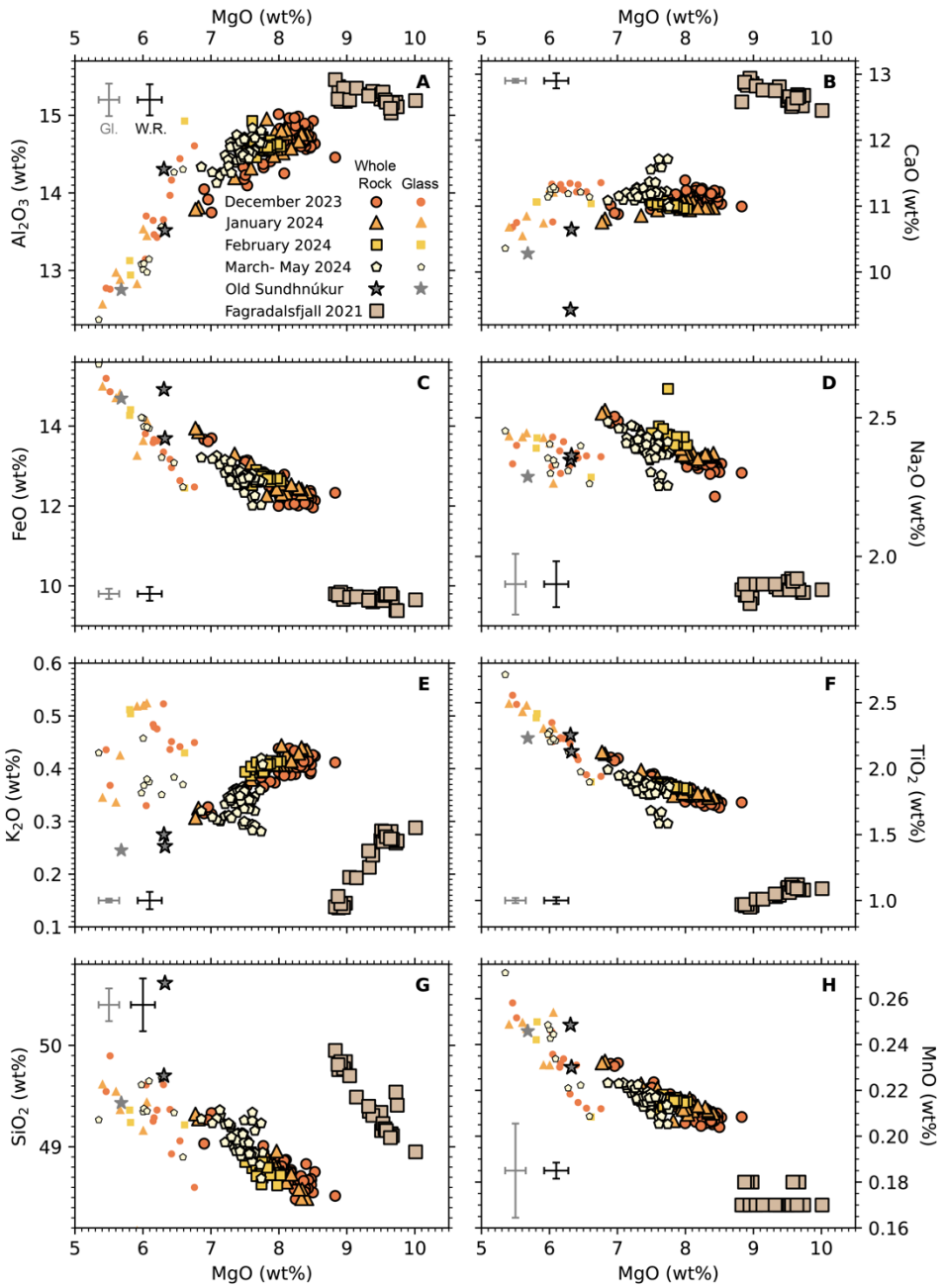

Fig. S3

The major element oxide concentrations for whole rocks and glasses from the Sundhnúksgígar eruptions compared with whole rock measurements from Fagradalsfjall 2021 (19) and old Sundhnúksgígar tephra. Each glass symbol shows the average of many EPMA analyses distributed across the sample. The error bars shown in black give the representative 2σ of repeat standard measurements across all ICP-OES sessions, and the accuracy is within this range. The grey error bars show 2σ of repeat standard measurements across all EPMA sessions of secondary standard material A99.

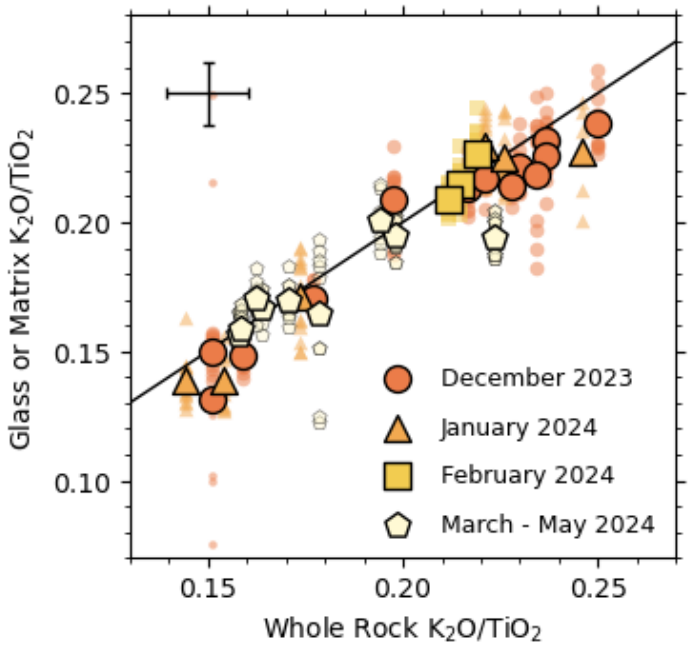

Fig. S4

Comparison of the K_2O/TiO_2 ratios measured on whole rock powders by ICP-OES and in-situ glass by EPMA. Small symbols show individual glass analyses, and large symbols show their mean. The small symbols at K_2O/TiO_2 ~0.15 are derived from measurements of a crystalline matrix with a defocused beam. The error bars are as described in the caption to Fig. S4. The solid line is a 1:1 line.

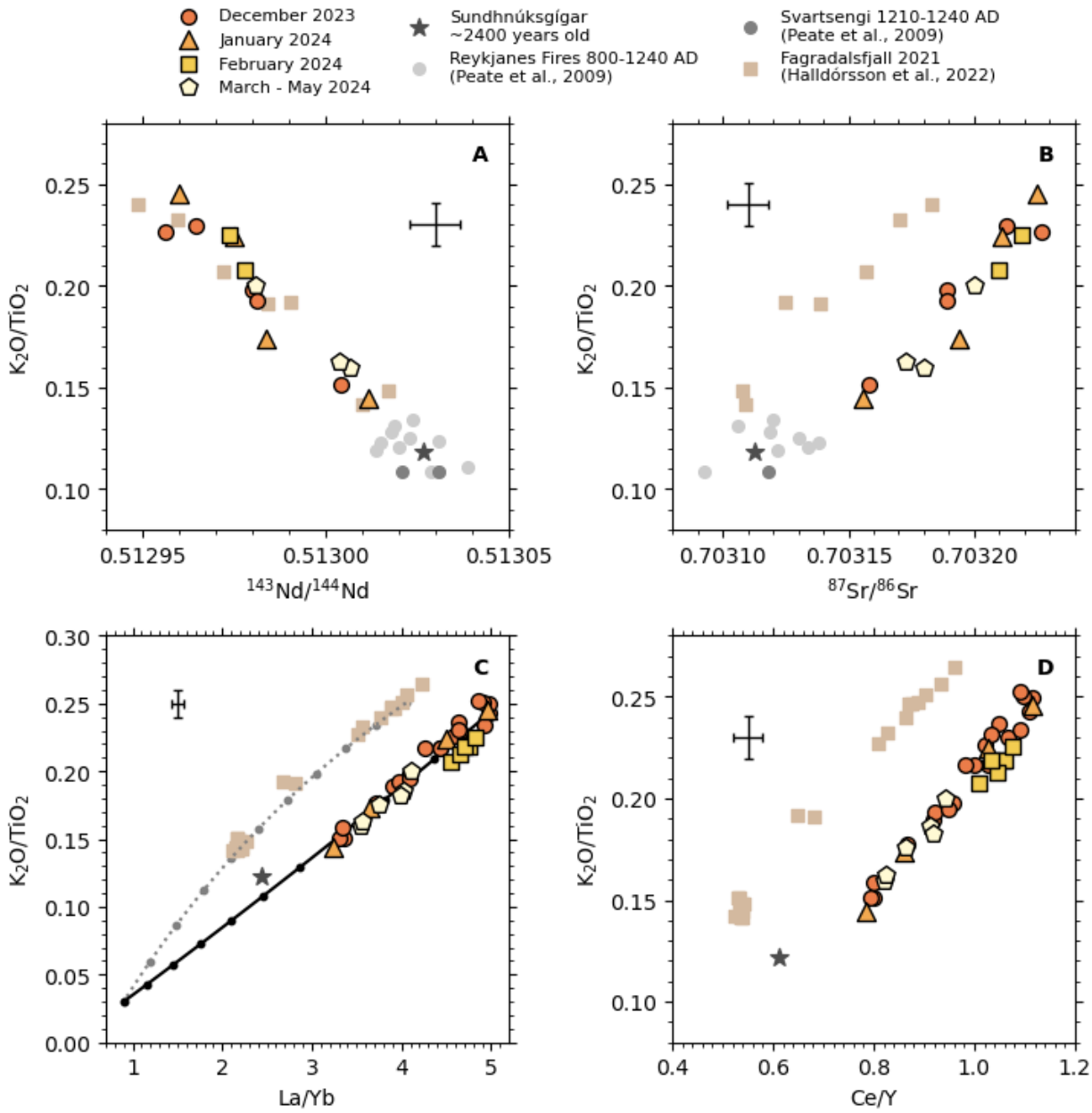

Fig. S5

Comparison of whole rock K_2O/TiO_2 with whole rock radiogenic isotope ratios and incompatible trace element ratios of picked glass. The error bars show the 2σ variability across measurement sessions, except for $^{87}Sr/^{86}Sr$ and $^{143}Nd/^{144}Nd$ where they are the maximum 2 s.e. calculated from the analyses. The lines in Panel (C) show the same mixing model as in Fig. S27B,C.

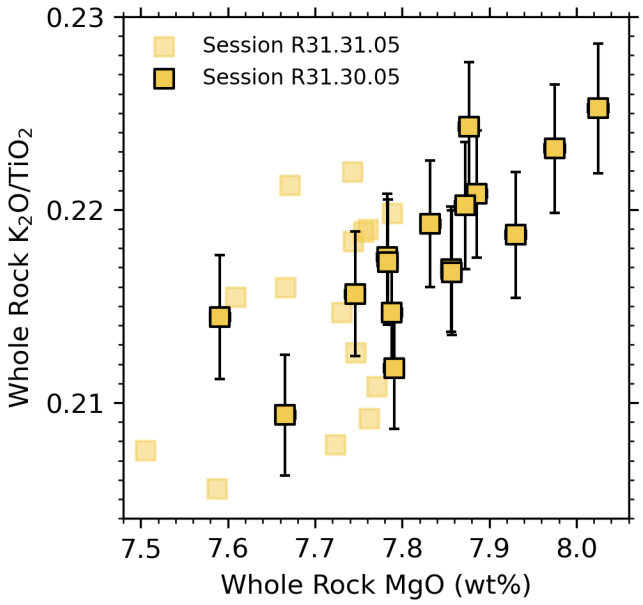

Fig. S6

The K_2O/TiO_2 ratios and MgO concentrations of the February lava and tephra. The analyses were performed over two sessions (R31.30.05 and R31.31.05). The internal precision of session R31.30.05 was sufficient to resolve variation in K_2O/TiO_2. The error bars show the estimated 2σ precision of the analyses on each sample analyzed in Session R31.30.05, using the precision on repeated BHVO-2 analyses (which was the least well reproduced standard in this session) and the formula $\sigma/\mu = \sigma_{BHVO2}/\mu_{BHVO2}/\sqrt{n}$, where n=2, the number of analyses of each sample, and μ is the mean. The precision of the MgO concentrations is smaller than the size of the symbol. The external accuracy is larger than the precision on the individual session and is better represented by the error bars on Fig. 2B of the main text.

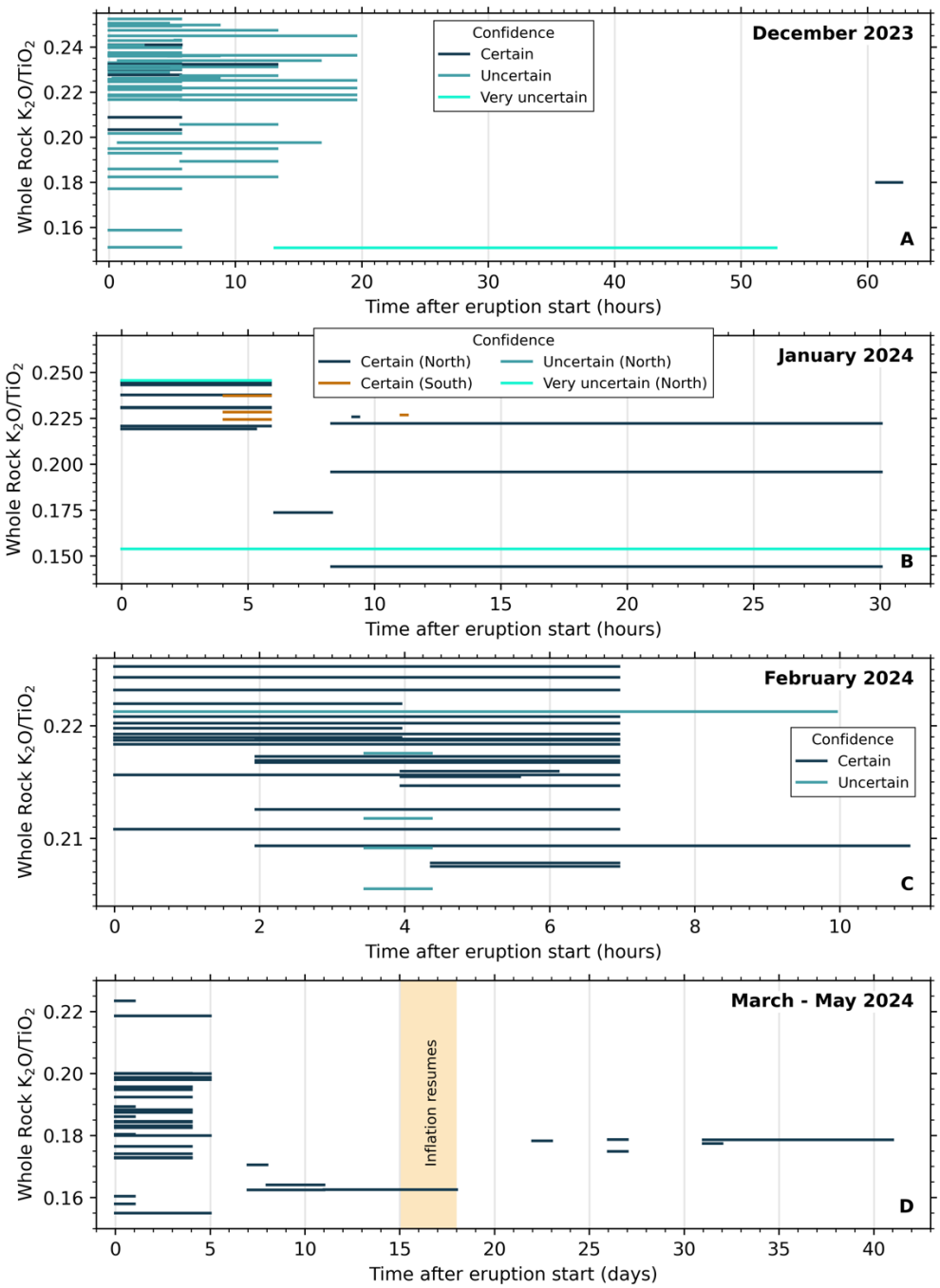

Fig. S7

Each line shows an individual lava or tephra sample and indicates the time window in which it was emplaced, alongside the whole rock K_2O/TiO_2 ratio. Qualitative indications of the certainty of these constraints are indicated by the color/shading of each line. Since eruption occurred from two distinct fissures in January, these samples are separated in panel (B). The yellow shading in (D) indicates when inflation resumed at Svartsengi following the start of the eruption. Since the time windows are courser in (D), the emplacement times are determined with more confidence.

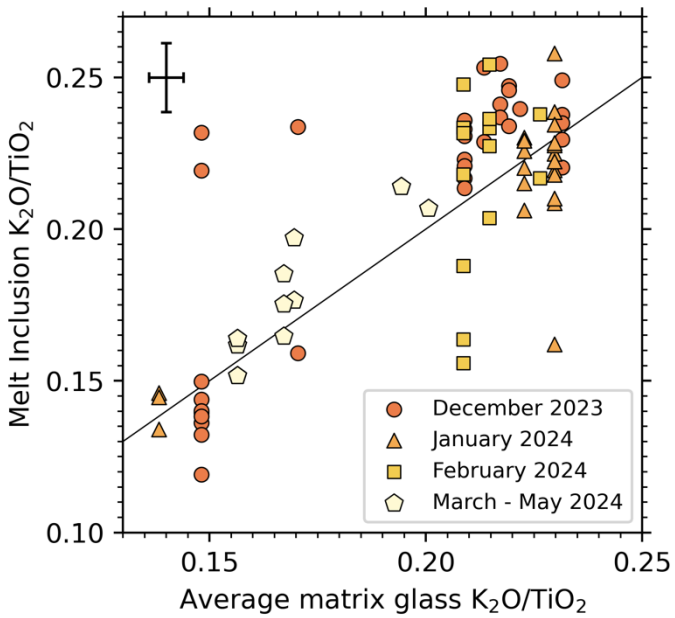

Fig. S8

The composition of individual olivine-hosted and plagioclase-hosted melt inclusions shown as a function of the average composition of the glass from their host rock. The solid line is a 1:1 line, showing the K_2O/TiO_2 ratios where the melt inclusions would have the same value as the glass in their host rock. The error shown for the melt inclusion measurements is the 2σ of repeated analyses of the secondary standard A99 across all sessions. The error shown for the average glass measurement is the 2σ of the session mean analysis of the A99 secondary standard.

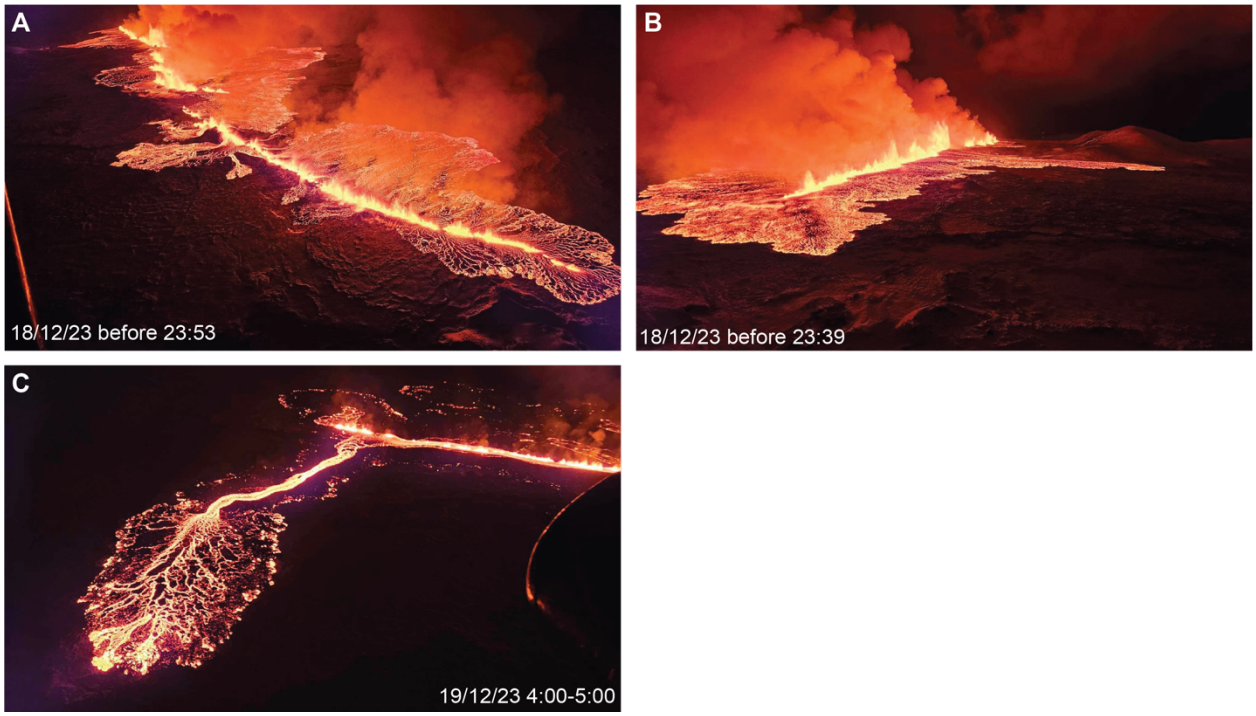

Fig. S9

Photos taken in the first hours of the December eruption during flights over the lava field. Photos courtesy of the Department of Civil Protection and Emergency Management, Iceland. (A) is taken from the southwest corner of the flow looking northeastwards. (B) is taken from the northeast corner of the flow, looking southwestwards. (C) is taken in the northwestern corner of the flow looking northeastwards.

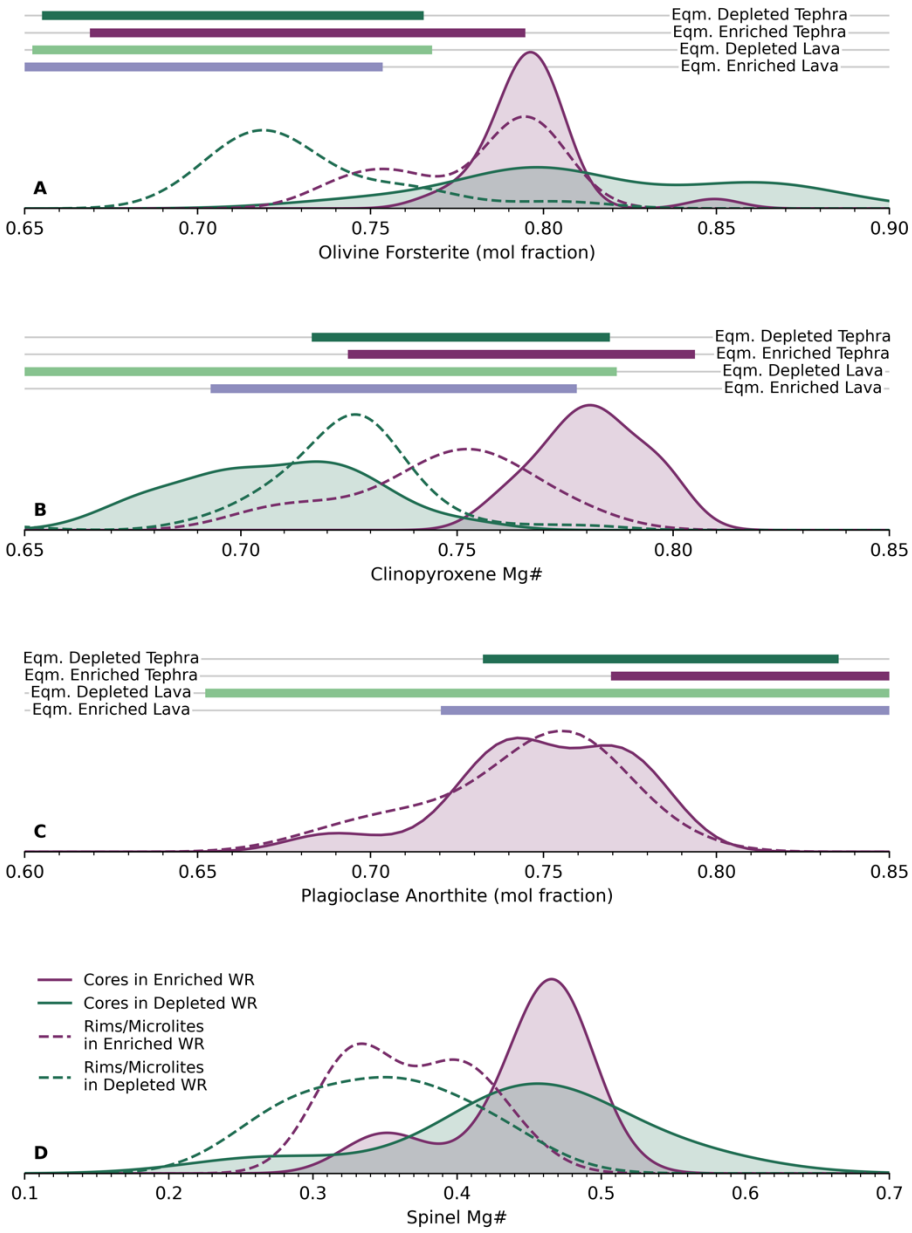

Fig. S10

Summary of olivine (A), clinopyroxene (B), plagioclase (C), and spinel (D) compositions, grouped into categories based on whole rock $K_2O/TiO_2 < 0.19$ (depleted) and $K_2O/TiO_2 > 0.19$ (enriched). The range in composition of olivine, clinopyroxene, and plagioclase predicted to be in equilibrium (marked Eqm. on the figure) with glass from the depleted and enriched tephra and lava are shown. The equilibrium olivine compositions were calculated assuming a Kd of 0.3. The equilibrium clinopyroxene compositions were calculated using the method by Wood & Blundy (*69*). The equilibrium plagioclase compositions were calculated using the method of Namur et al. (*70*). The individual analyses are shown vs whole rock K_2O/TiO_2 in fig. S28.

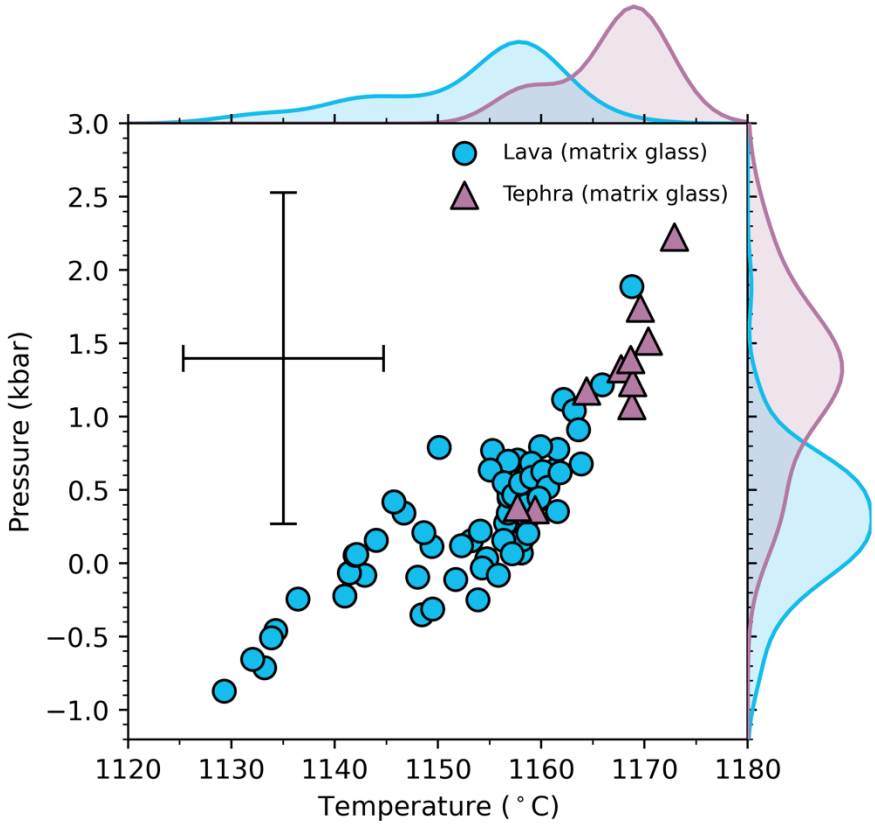

Fig. S11

Equilibration temperatures and pressures of lava and tephra glass calculated using the OPAM geothermobarometer (30). Only results where the estimated probability of three-phase saturation was > 0.8 are shown. The error bars show the mean absolute error of the parameterization (1,*57*).

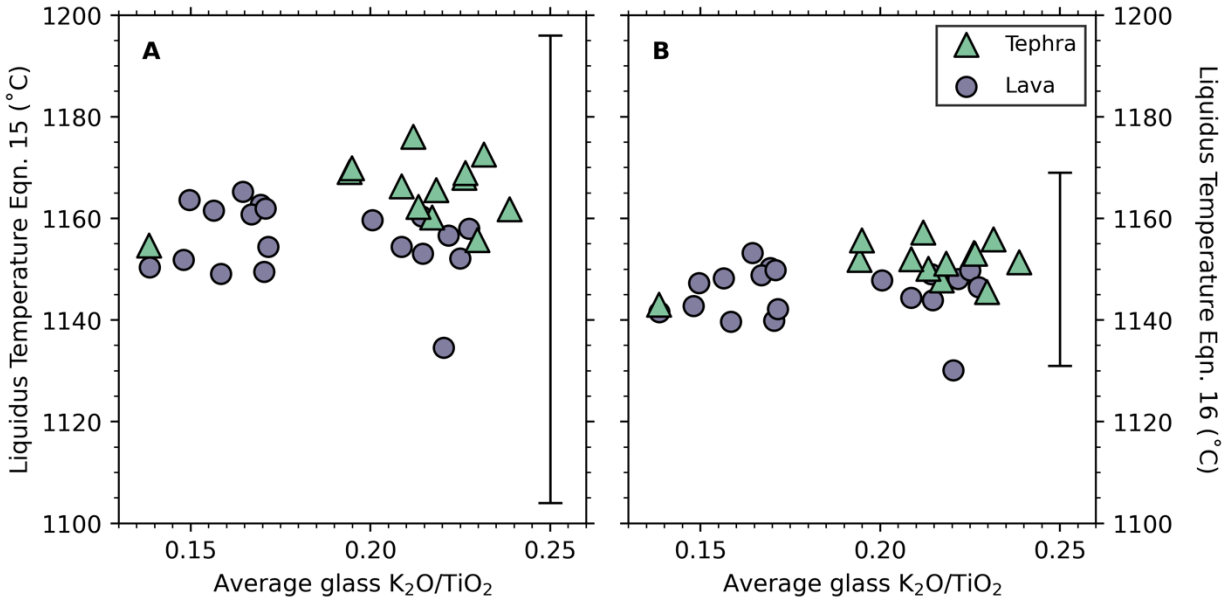

Fig. S12

Liquidus temperatures calculated using (A) parameterizations of olivine-saturated (Eqn. 15) and (B) olivine-clinopyroxene-plagioclase-saturated (Eqn. 16) experiments (*60*), using the mean major element oxide concentrations in glass from each sample. The error bars show the reported uncertainty on the thermometer (*60*). Error bars for K_2O/TiO_2 are omitted.

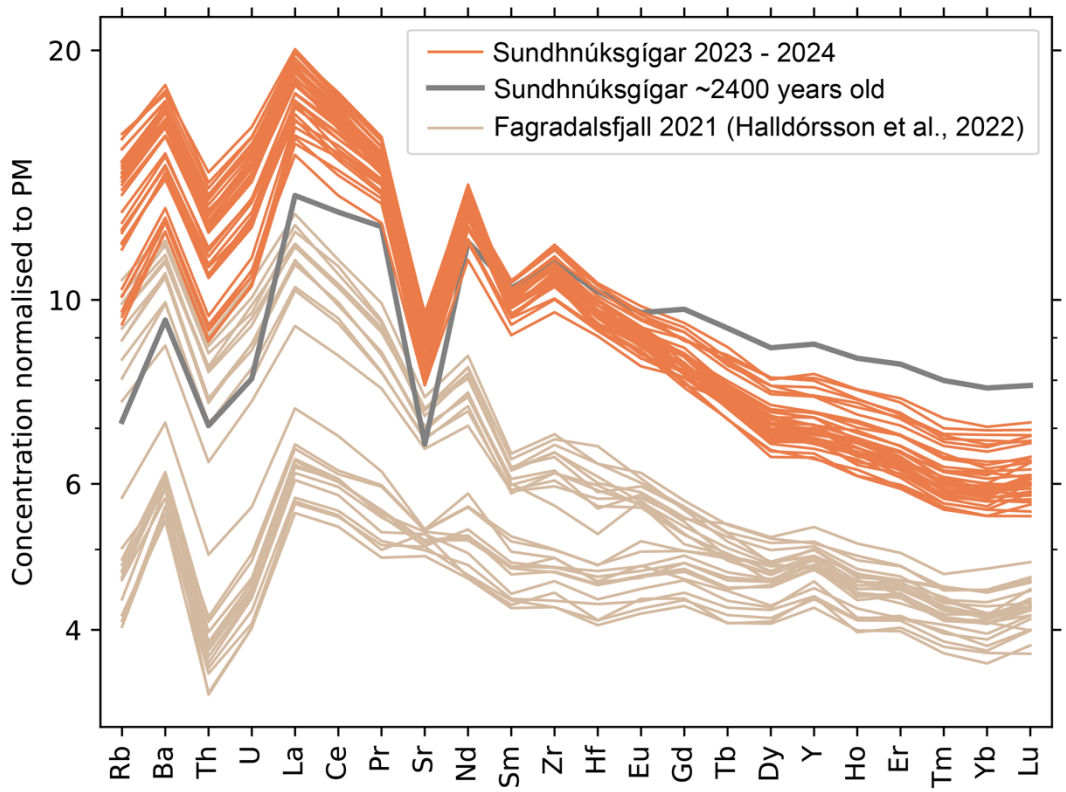

Fig. S13

Comparison of the trace element concentrations in the Sundhnúksgígar 2023-2024 eruptions with Fagradalsfjall 2021 (19) and the lava erupted ~2400 years ago at Sundhnúksgígar. Each line represents a single sample. The concentrations are normalized to the composition of the primitive mantle (*71*).

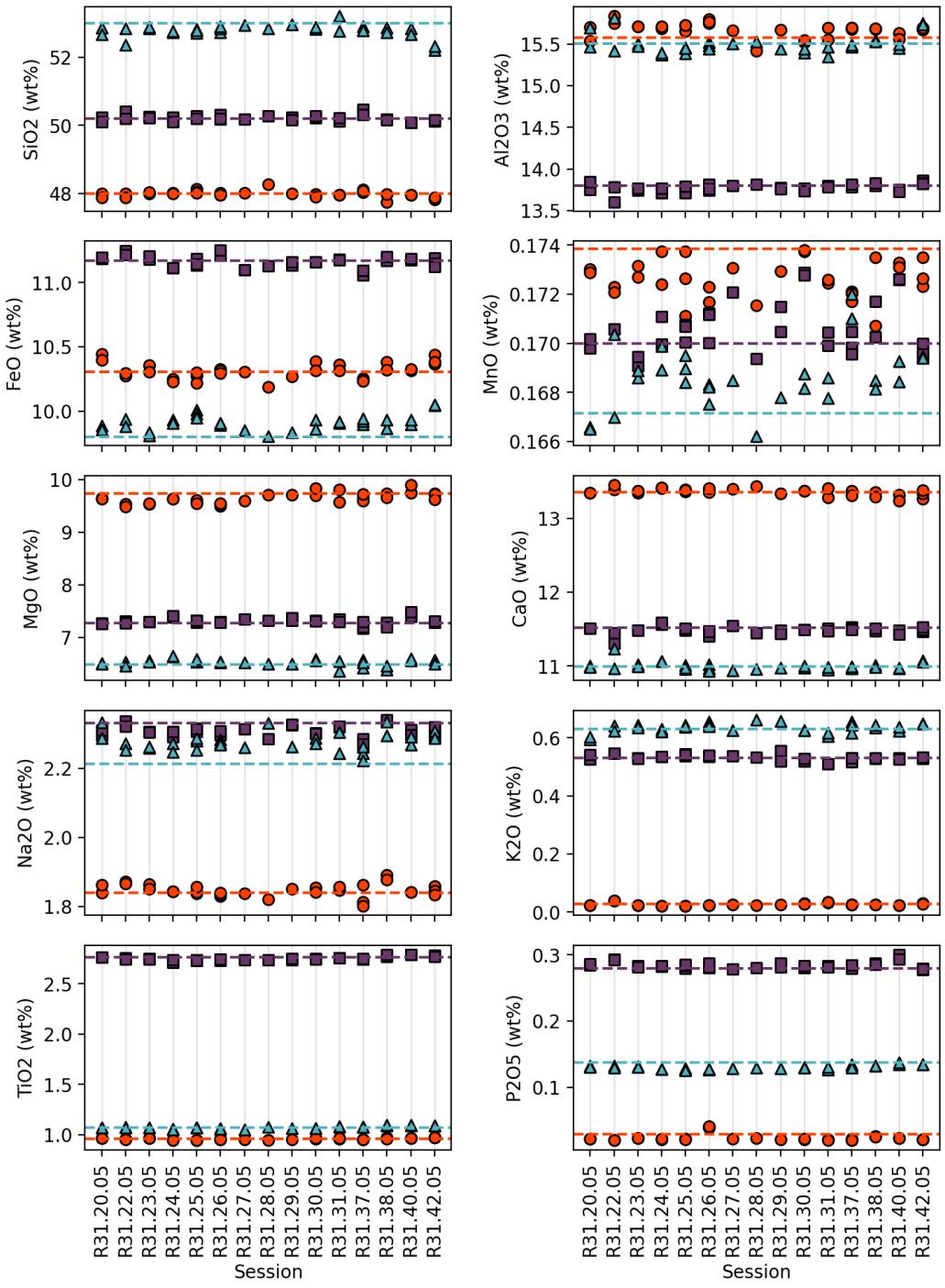

Fig. S14

Summary of the standard analyses during each ICP-OES session. The horizontal dashed lines show the GEOREM (*55*) preferred values. The red circles are BIR-1, the light blue triangles are W2, and the dark blue squares are BHVO-1.

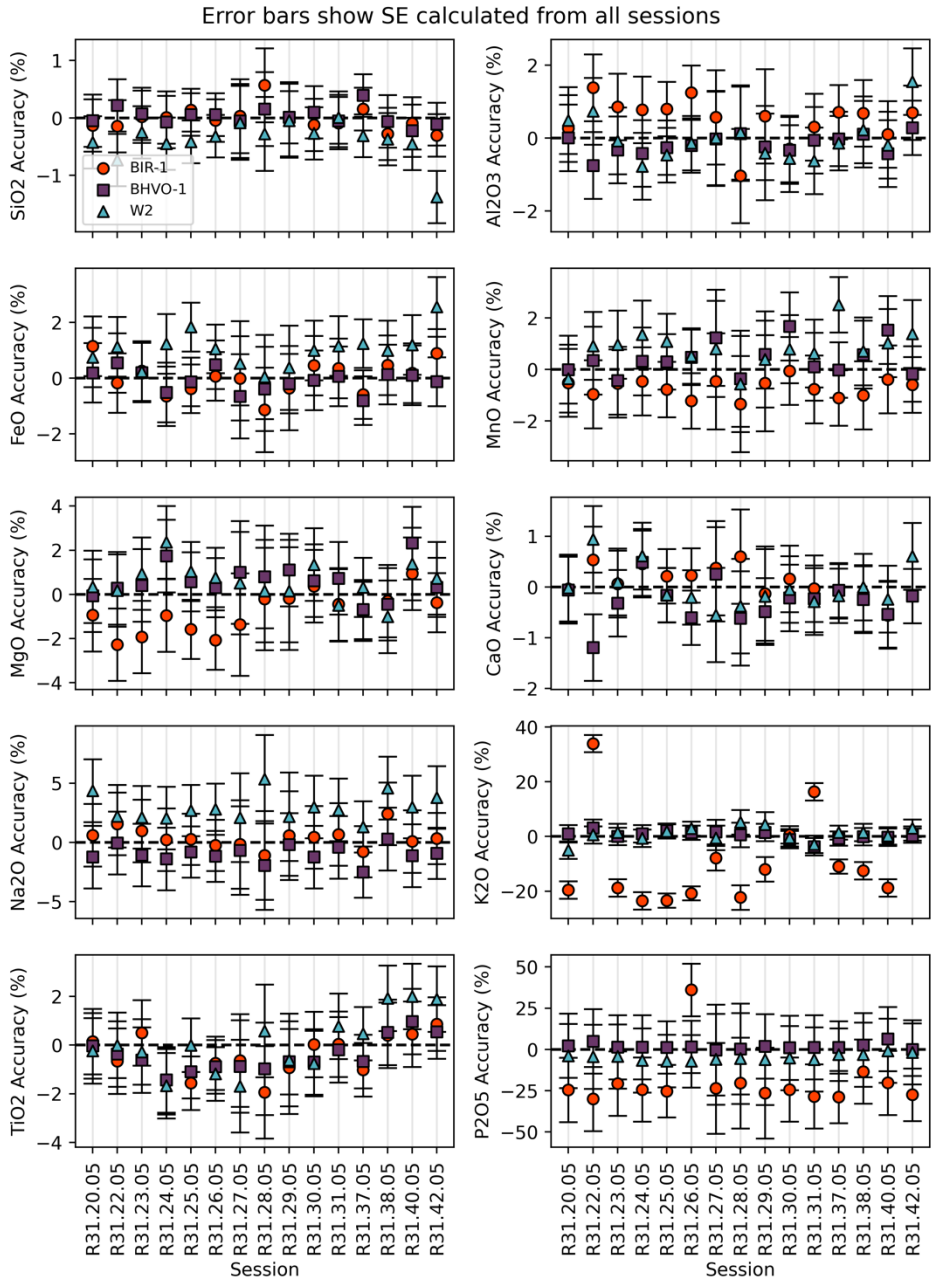

Fig. S15

Summary of the relative accuracy of the standard measurements during each ICP-OES session. The error bars show the relative standard error in the mean across all standards and sessions. For K_2O, the standard error does not include BIR-1 as the K_2O concentration is much lower than the other standards and all sample measurements reported here.

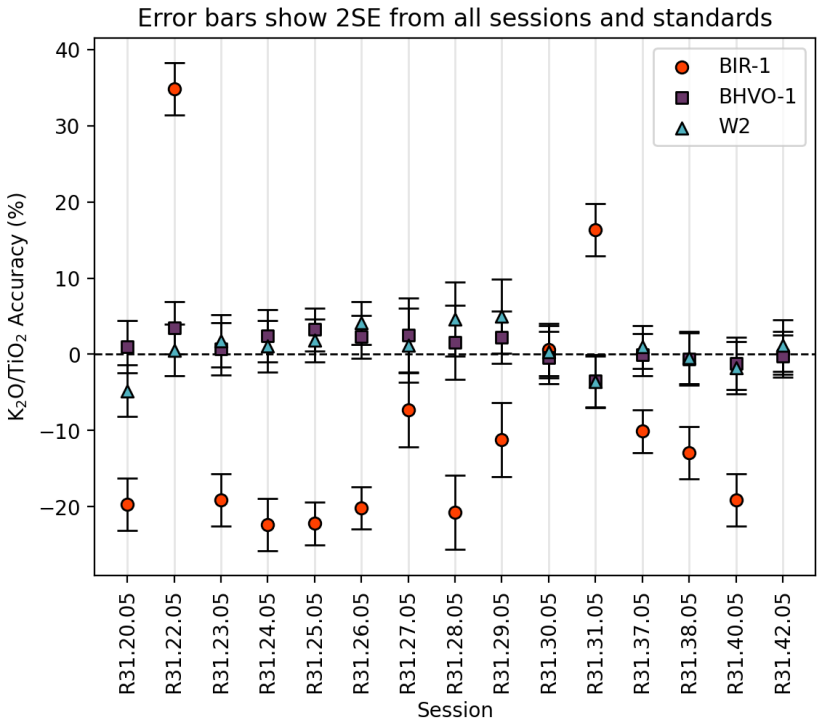

Fig. S16

Summary of the relative accuracy of the K_2O/TiO_2 ratio during each ICP-OES session. The error bars show the relative standard error in the mean for BHVO and W2 across all sessions. The standard error was calculated without BIR-1 as the K_2O concentration is much lower than the other standards and all sample measurements reported here.

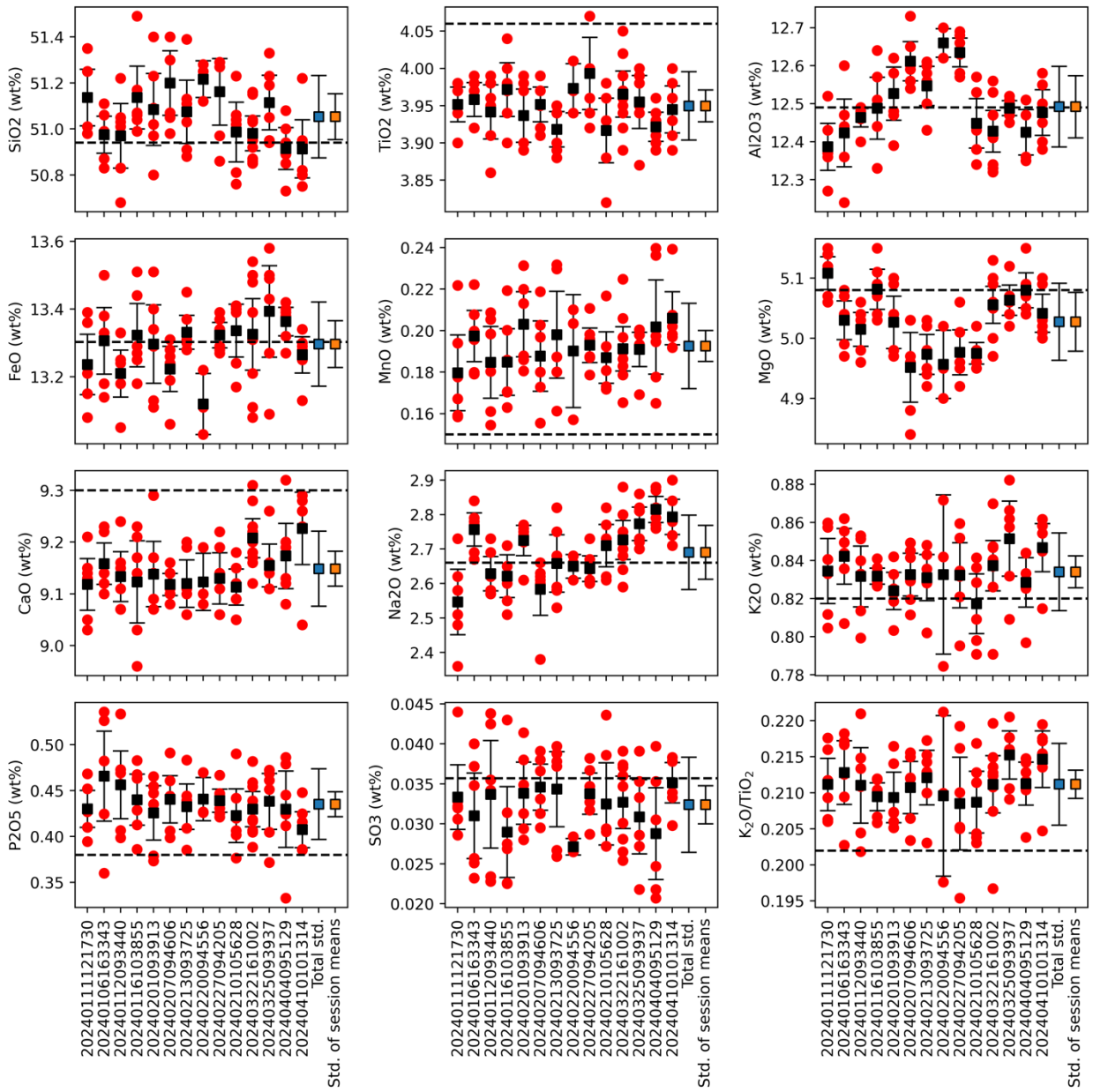

Fig. S17

Summary of repeated electron-probe analyses of secondary standard material A99. The red circles show individual analyses, the black squares show the session mean, and their error bars show 2s.e. in the mean. The horizontal dashed lines show the accepted values.

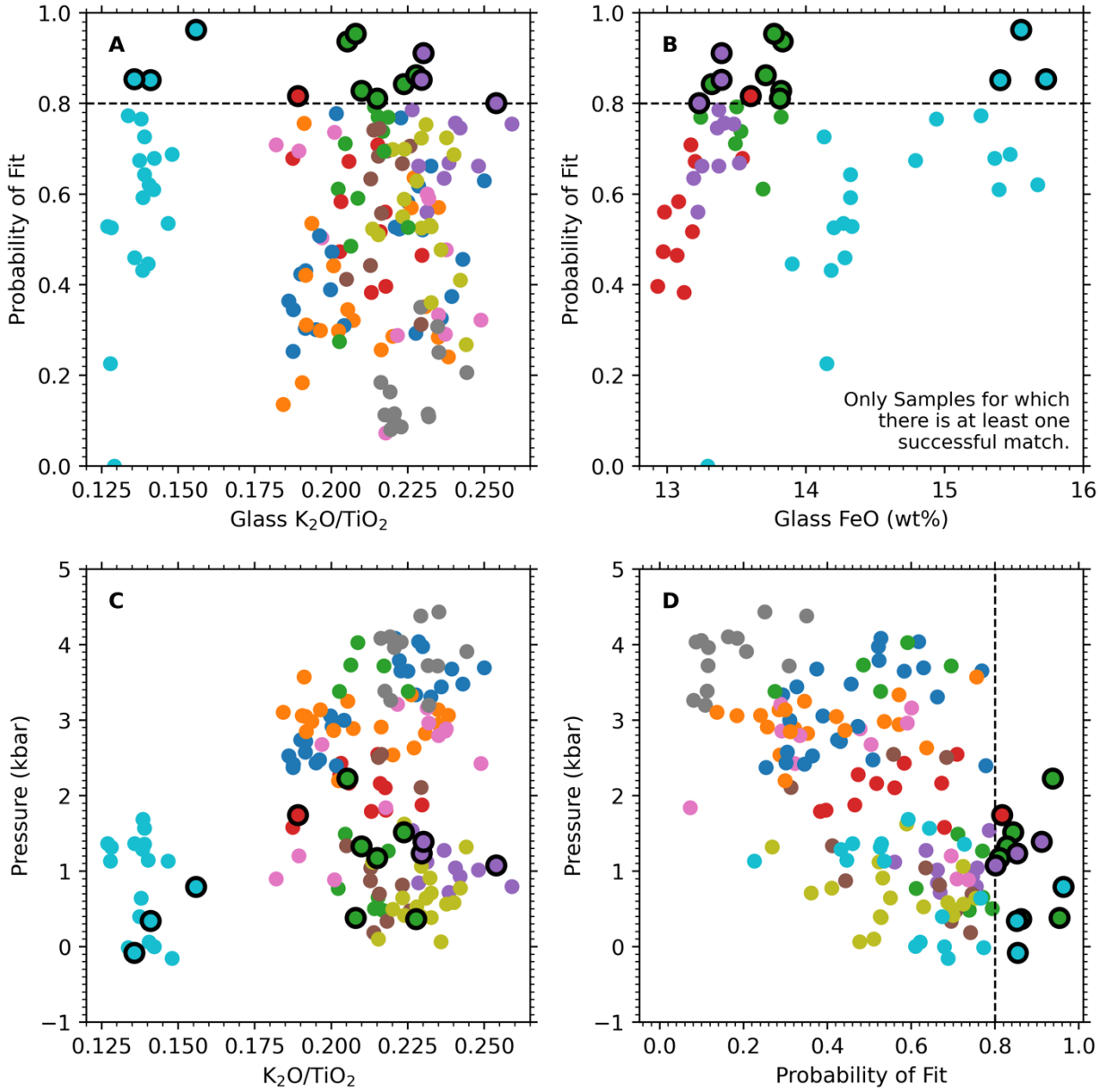

Fig. S18

Results of the tephra OPAM calculations, including glass analyses that had a low probability of fit. The symbols outlined in bold show the analyses with a probability of fit > 0.8, which are the pressures shown in Fig. 3. Glass analyses from the same sample are shown with the same color.

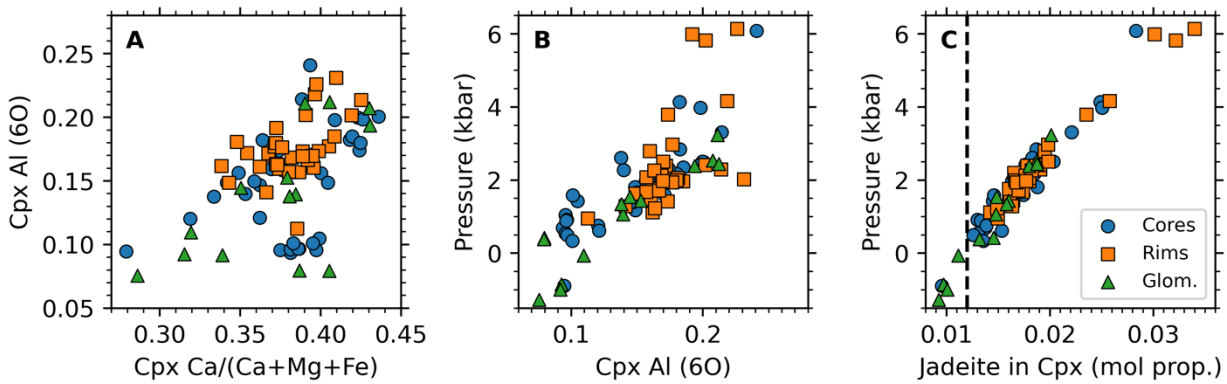

Fig. S19

Results of the clinopyroxene-liquid calculations, including results that are filtered out on the basis of low jadeite contents. The threshold for filtering is shown by the dashed line in panel (C).

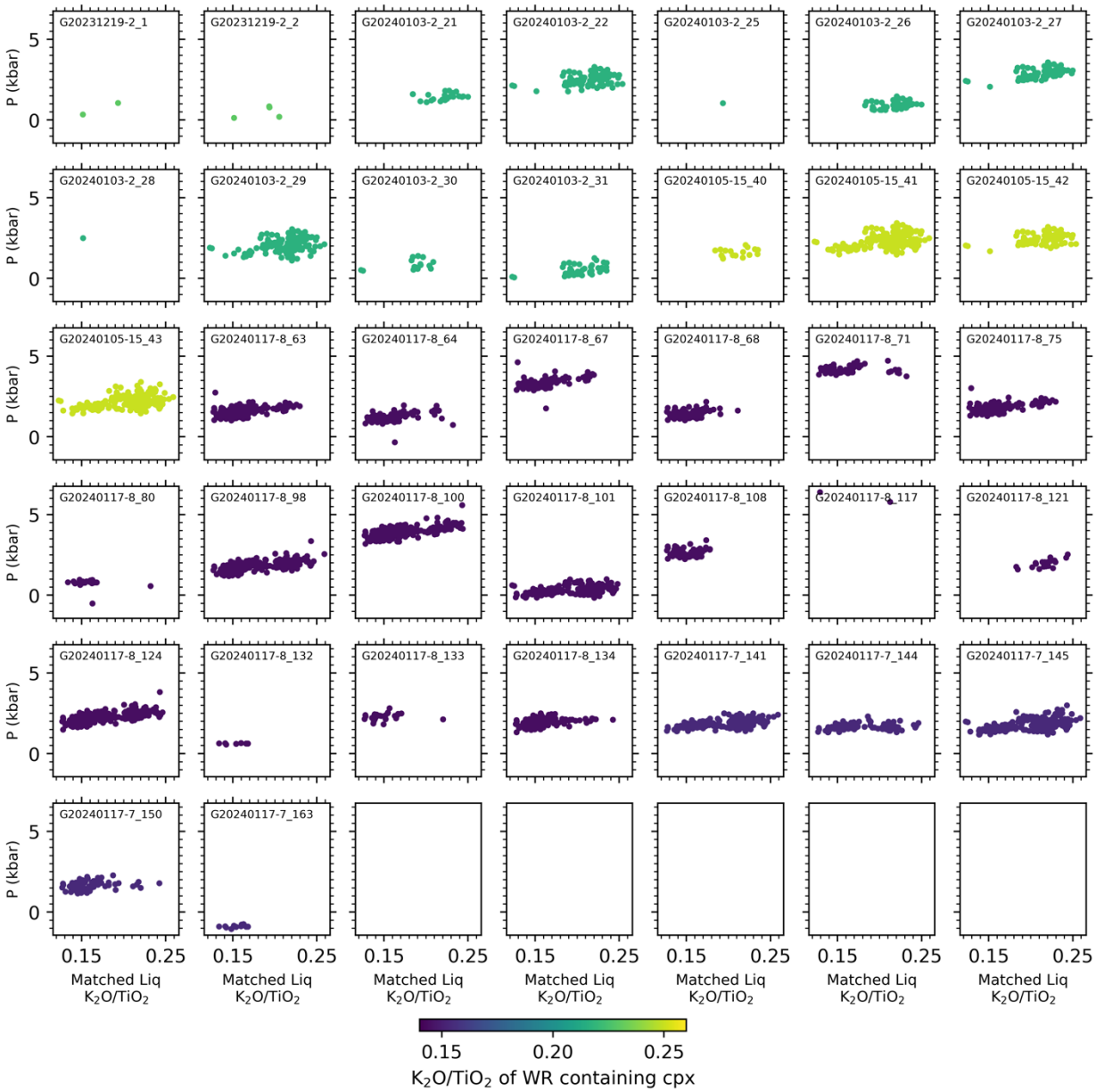

Fig. S20

Results of clinopyroxene-liquid geobarometry calculations for clinopyroxene cores. Each panel shows an individual clinopyroxene core analysis, and the symbols show the K_2O/TiO_2 of the glass compositions identified as potential equilibrium matches and the pressure for each liquid-pyroxene pair.

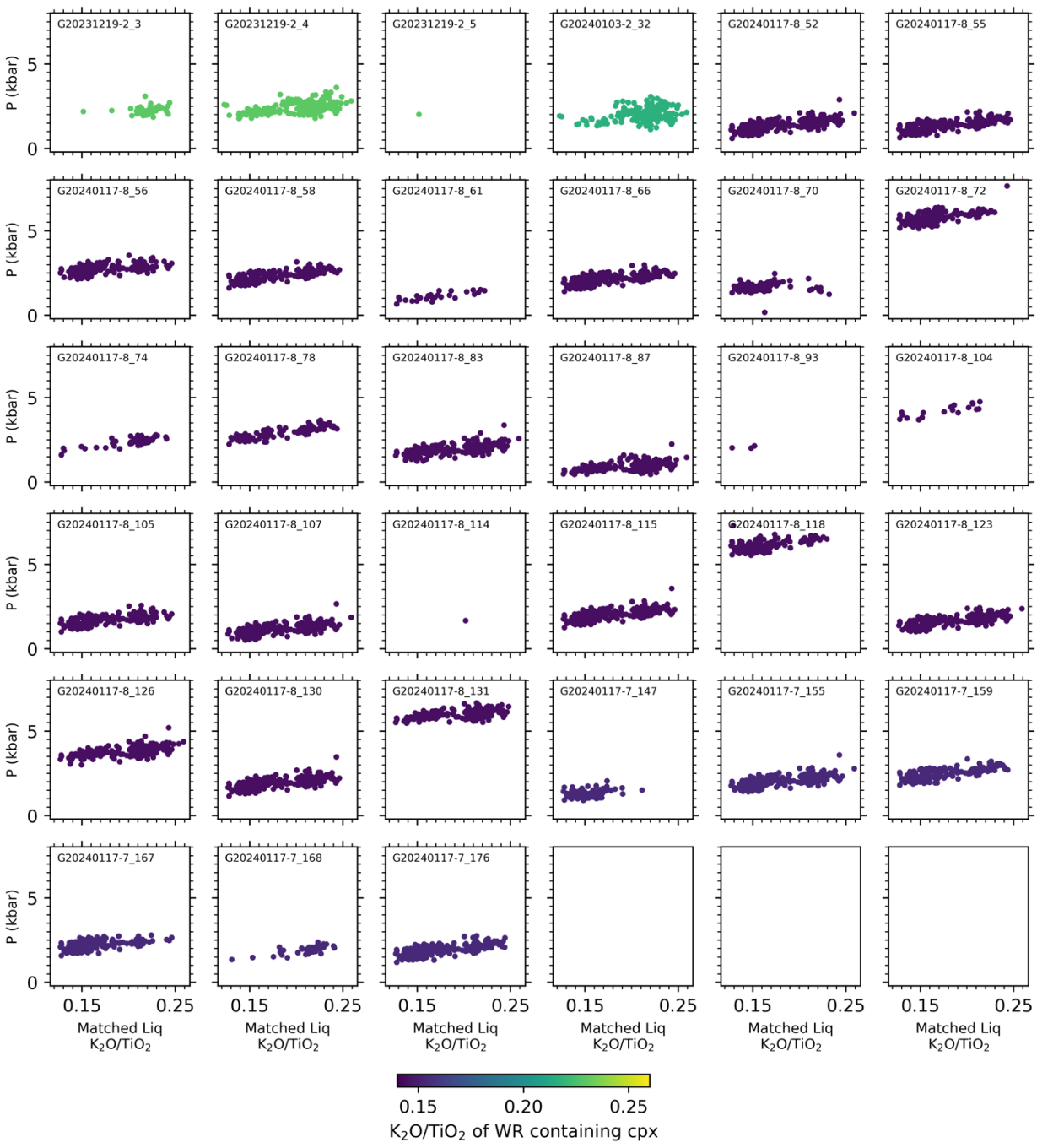

Fig. S21

Results of clinopyroxene-liquid geobarometry calculations for clinopyroxene rims. Each panel shows an individual clinopyroxene rim analysis, and the symbols show the K_2O/TiO_2 of the glass compositions identified as potential equilibrium matches and the pressure for each liquid-pyroxene pair.

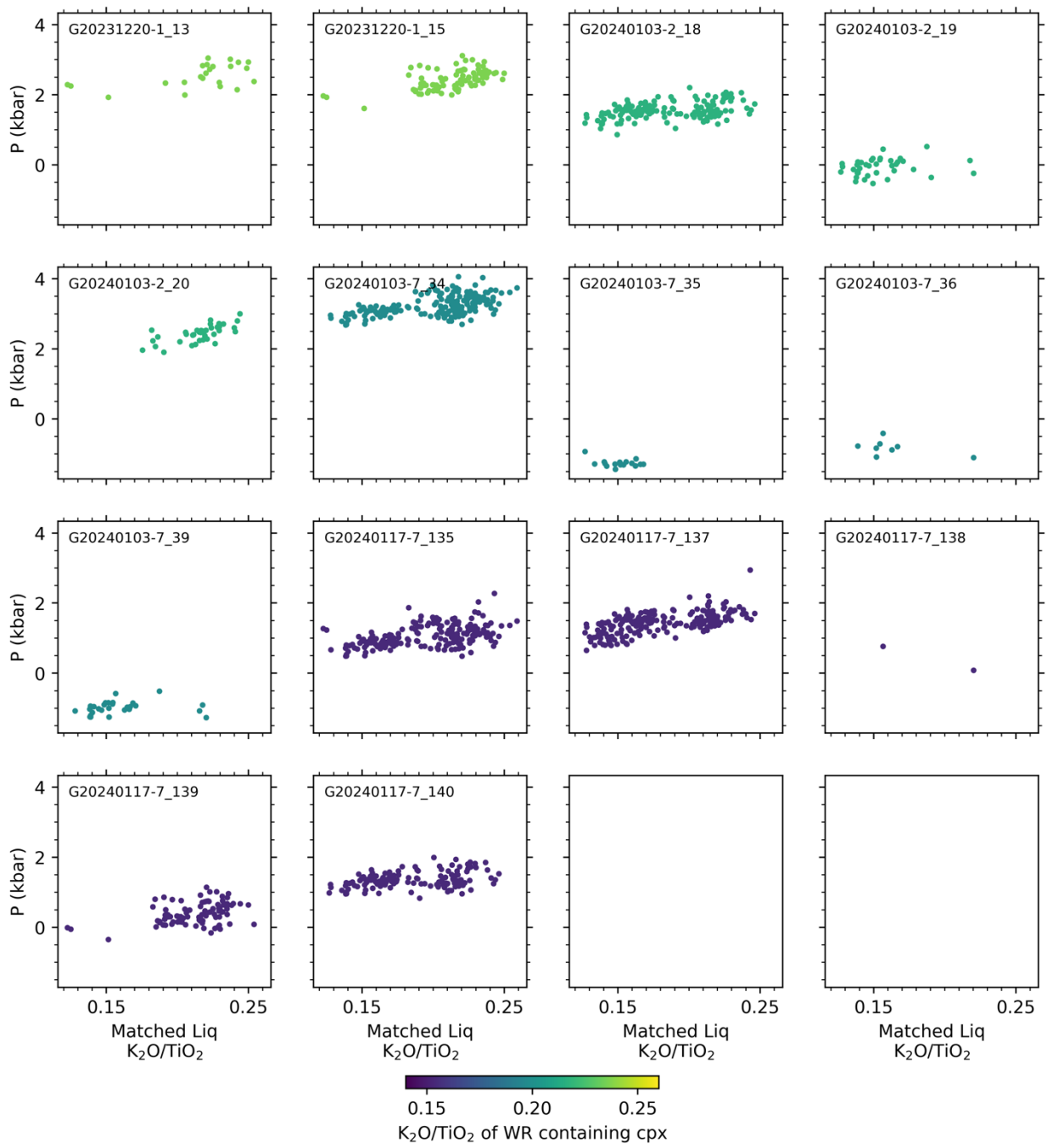

Fig. S22

Results of clinopyroxene-liquid geobarometry calculations for clinopyroxene glomerocrysts. Each panel shows an individual clinopyroxene glomerocryst analysis, and the symbols show the K_2O/TiO_2 of the glass compositions identified as potential equilibrium matches and the pressure for each liquid-pyroxene pair.

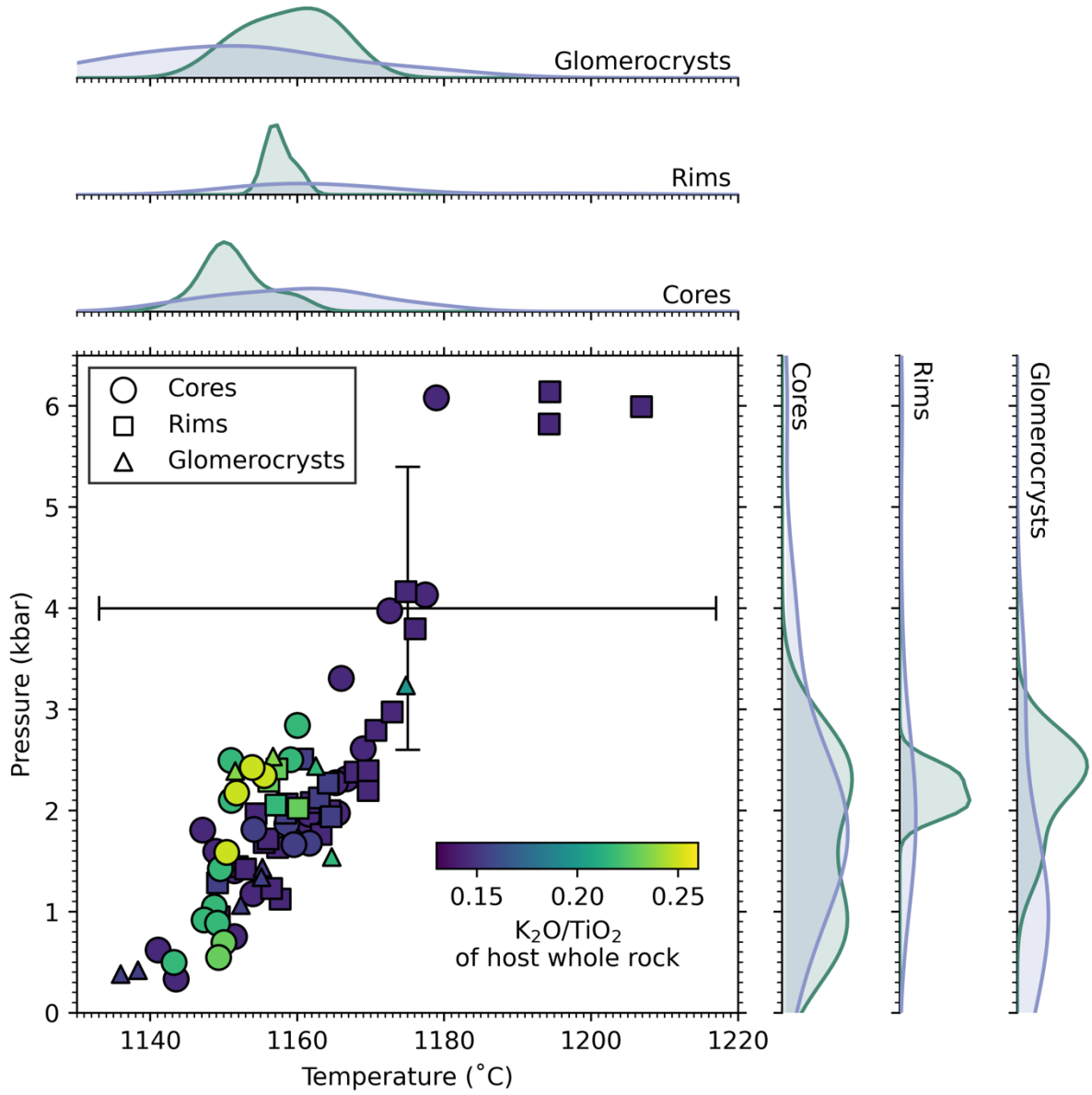

Fig. S23

Results of applying the clinopyroxene-liquid geothermobarometer (29,50). Each symbol indicates the mean temperature and pressure calculated from a single clinopyroxene analysis and all matched liquids. The shading of the symbols shows the K_2O/TiO_2 ratio of the whole rock whence the crystals derived. The kernel density estimates show pressures and temperatures grouped according to whether the whole rock has $K_2O/TiO_2 < 0.19$ (depleted, blue) or $K_2O/TiO_2 > 0.19$ (enriched, green). The error bars show the reported uncertainty of the geothermobarometer.

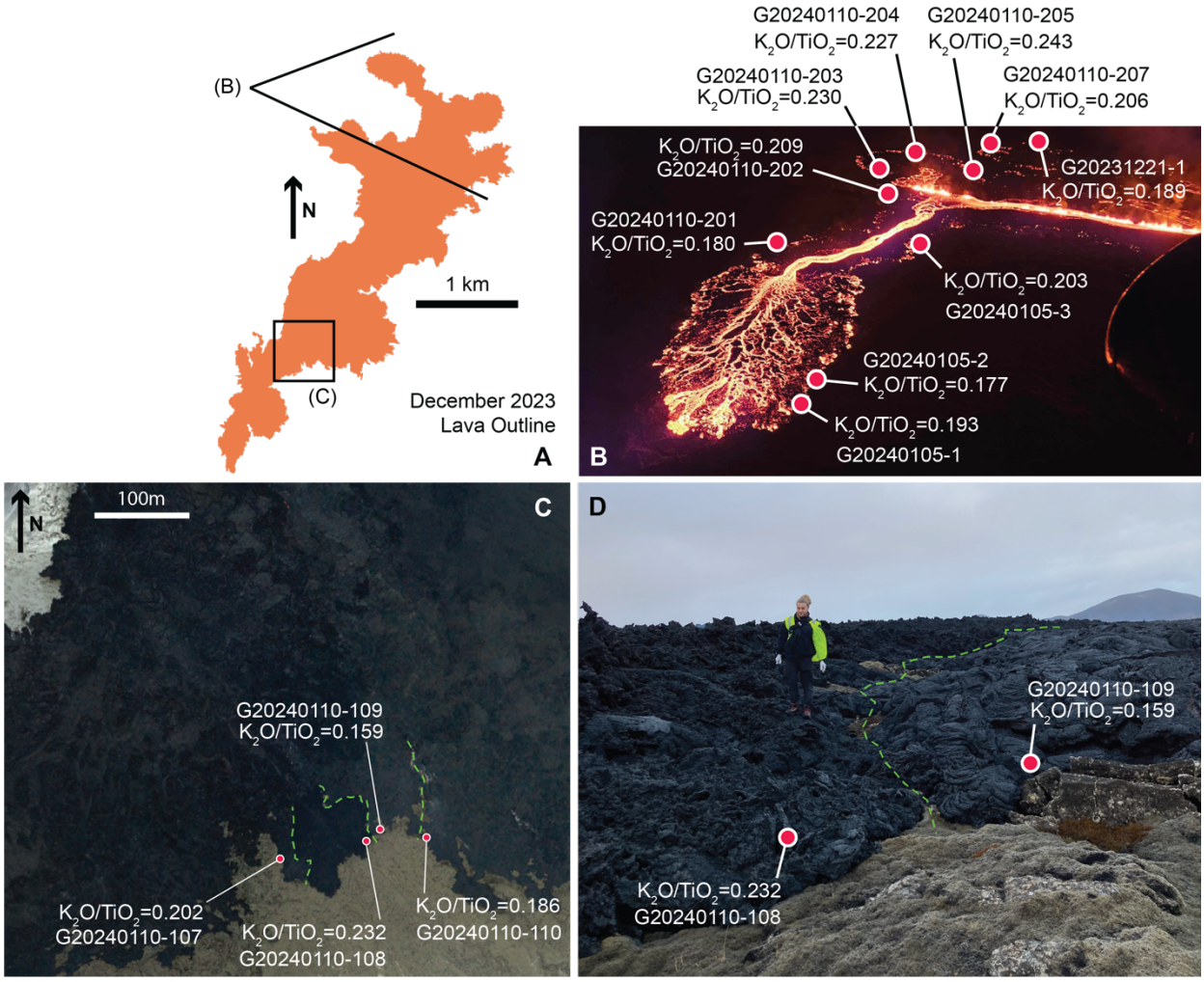

Fig. S24

Examples of the spatial variation in K_2O/TiO_2 from the December 2023 eruption. (A) shows the outline of the lava from December 2023 and the approximate field of view of the aerial photo in (B) and the region shown in (C). (B) is the same photo as shown in Fig. S7 and is overlain with the indicative location of samples taken in the northernmost part of the lava field alongside the whole rock K_2O/TiO_2 ratio. (C) is an aerial photo of a region near the southern extent of the lava field with contacts between individual flow units indicated with dashed green lines. The locations of samples and their whole rock K_2O/TiO_2 ratios are indicated. The aerial photo is from the Reykjanes orthomosaics published by the National Land Survey of Iceland (obtained on 21 December 2023) and downloaded in January 2024. (D) shows a photo of one of the contacts shown in (C) with the approximate sample locations indicated.

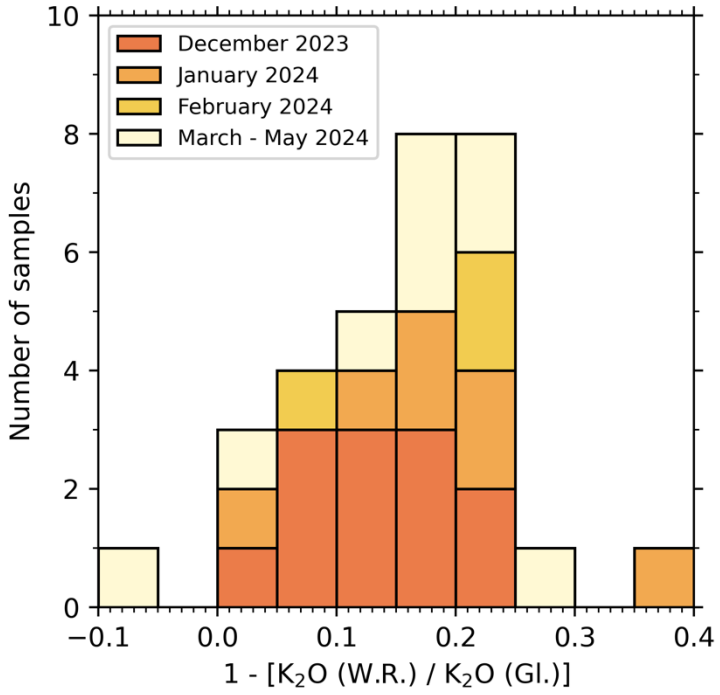

Fig. S25

Estimated crystallinity (by mass) of samples where both whole rock powders and in-situ glass major element analyses were obtained. The x-axis gives the crystallinity under the assumption that K_2O behaves as a perfectly incompatible element.

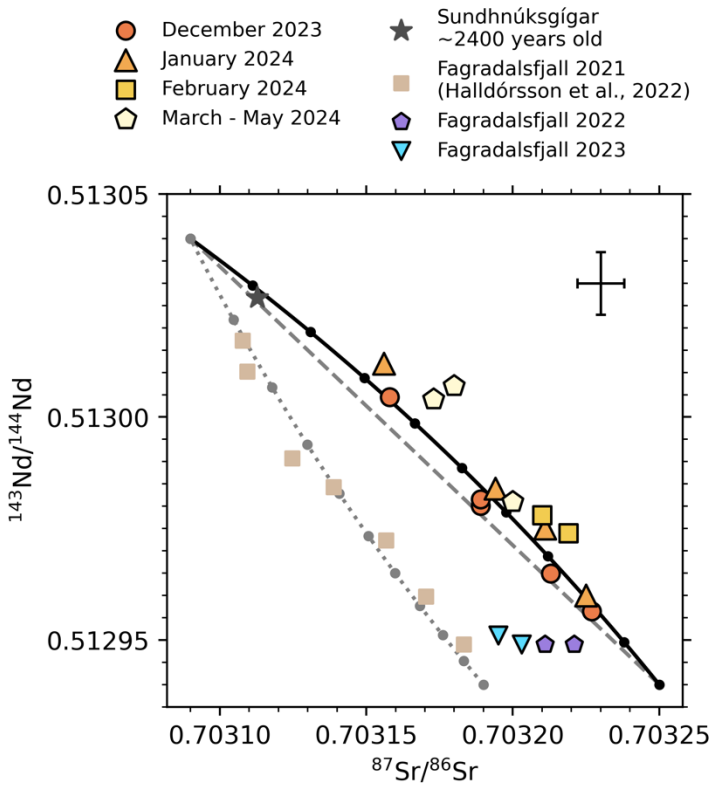

Fig. S26

Illustrative mixing models for Sr-Nd between the depleted and enriched endmembers. The solid line shows the model for the Sundhnúksgígar eruptions. The dashed line is the mixing line for endmembers with the same $^{87}Sr/^{86}Sr$ and $^{143}Nd/^{144}Nd$ ratios but Sr and Nd concentrations required to match the Fagradalsfjall 2021 Sr and Nd concentrations (fig. S27). The dotted line shows the model for the Fagradalsfjall 2021 lavas. Increments of 10% mixing are shown by the circles. The mixing lines are chosen to illustrate where a single depleted endmember would sit (see supplementary text). See the caption to Fig. 2 for information about the symbols and error bars. The mixing model parameters are given in Table S6.

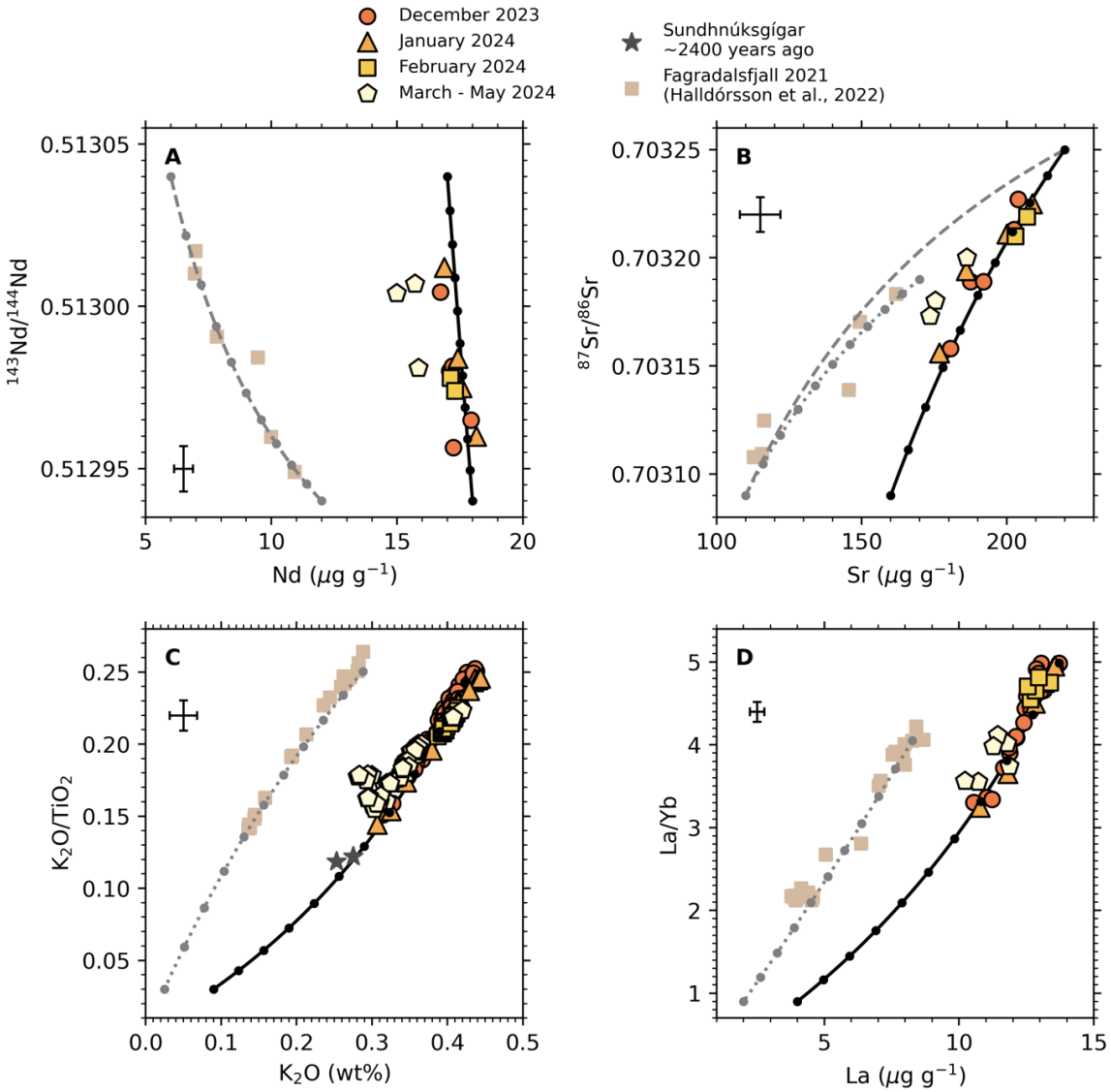

Fig. S27

Illustrative mixing models between the depleted and enriched endmembers. Panels (A) and (B) show mixing models that match the Sr-Nd systematics, and panels (C) and (D) show different models that match the K_2O-TiO_2-La-Yb systematics. The solid lines show the mixing models for the December – February Sundhnúksgígar eruptions. The March-May 2024 data falls off the arrays, possibly due to greater crystallinity diluting the trace element concentrations. The dashed lines in panels (A) and (B) are mixing lines for endmembers with the same $^{87}Sr/^{86}Sr$ and $^{143}Nd/^{144}Nd$ ratios but Sr and Nd concentrations required to match the Fagradalsfjall 2021 Sr and Nd concentrations. This is the same model as shown by the dashed line in fig. S26. The dotted line shows the model for the Fagradalsfjall 2021 lavas. Increments of 10% mixing are shown by the circles. The mixing lines are chosen to illustrate where a single depleted endmember would sit (see supplementary text). Notice the models in (A) and (B) have inconsistent mixing proportions with the models in (C) and (D). The mixing model parameters are given in Tables S6 and S7.

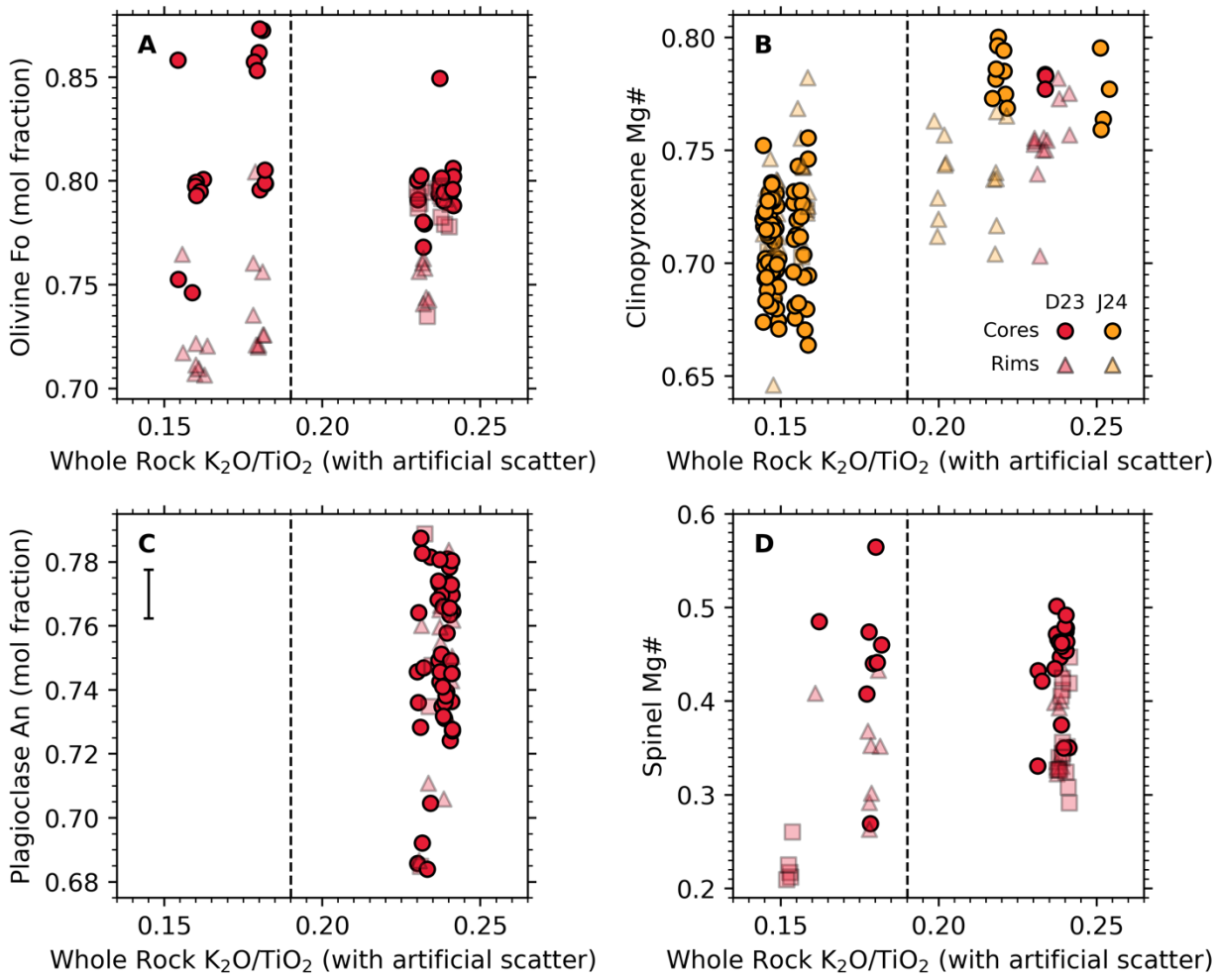

Fig. S28

Individual electron probe analyses of olivine (A), clinopyroxene (B), plagioclase (C), and spinel (D). The compositions are plotted at the K_2O/TiO_2 of the whole rock from which the crystal was derived. The dashed line shows the cut-off between depleted and enriched populations shown in Fig. S10. The 2σ uncertainty on the analyses are on the order of the symbol size, except for plagioclase An, the uncertainty for which is indicated by the error bar on panel (C).

Element	Spec	Crystal	Standard	Peak (sec)	Backgr. (sec)
Si	1	TAP	Tectite Glass (NMNH 2231) / Rhyolite Glass VG-568 (NMNH 72854)	30	10
Ti	2	PETJ	Hornblende (Kakanui) (NMNH 143965)	40	20
Al	1	TAP	Anorthite (NMNH 137041)	30	15
Fe	4	LIFL	Gl401 (basaltic glass from P. Roeder)	40	20
Mn	4	LIFL	Bustamite (Astimex Standards Ltd.)	40	20
Mg	5	TAP	Diopside Glass (NASA)	30	15
Ca	2	PETJ	Diopside Glass (NASA)	30	15
Na	5	TAP	Omphacite (NMNH 110607)	20	10
K	2	PETJ	Corning Glass D (NMNH 117218-3)	40	20
P	2	PETJ	Apatite (Astimex Standards Ltd.)	40	20
S	3	PETH	Pyrite (Astimex Standards Ltd.)	120	60
Cl	3	PETH	Scapolite (Meionite) (NMNH R6600)	90	90

Table S1.

Standards, spectrometers and analytical crystals used, and counting times on peak and background on each side of peak for S- and Cl-bearing basalt glass analyses.

Element	Spec	Crystal	Standard	Peak (sec)	Backgr. (sec)
Si	1	TAP	Olivine (San Carlos) (NMNH 111312-44)	30	15
Ti	2	PETJ	Hornblende (Kakanui) (NMNH 143965)	30	30
Al	1	TAP	Pyrope (NMNH 143968)	30	30
Fe	3	LIFH	Fayalite (NMNH 85276)	30	15
Mn	4	LIFL	Bustamite (Astimex Standards Ltd.)	30	30
Mg	5	TAP	Olivine (Astimex Standards Ltd.)	30	15
Ca	2	PETJ	Diopside (NMNH 117733)	30	15
Cr	4	LIFL	Chromite (NMNH 117075)	30	30
Ni	3	LIFH	Pentlandite (Astimex Standards Ltd.)	30	30

Table S2.
Standards, spectrometers and analytical crystals used, and counting times on peak and background on each side of peak for olivine analyses.

Element	Spec.	Crystal	Standard	Peak (sec)	Backgr. (sec)
Si	1	TAP	Pyrope (NMNH 143968)	30	30
Ti	2	PETJ	Rutile (Astimex Standards Ltd.)	40	20
Al	1	TAP	Pyrope (NMNH 143968)	30	15
Fe	3	LIFH	Hematite (Astimex Standards Ltd.)	30	15
Mn	4	LIFL	Bustamite (Astimex Standards Ltd.)	30	30
Mg	5	TAP	Chromite (NMNH 117075)	30	30
V	4	LIFL	Vanadium (metal) (Astimex Standards Ltd.)	30	30
Cr	4	LIFL	Chromite (NMNH 117075)	30	15
Ni	3	LIFH	Pentlandite (Astimex Standards Ltd.)	40	20

Table S3.
Standards, spectrometers and analytical crystals used, and counting times on peak and background on each side of peak for spinel analyses.

Element	Spec.	Crystal	Standard	Peak (sec)	Backgr. (sec)
Si	1	TAP	Plagioclase (NMNH 115900)	40	20
Ti	2	PETJ	Hornblende (Kakanui) (NMNH 143965)	40	40
Al	1	TAP	Anorthite (NMNH 137041)	40	20
Fe	3	LIFH	Hornblende (Kakanui) (NMNH 143965)	40	20
Mn	3	LIFH	Bustamite (Astimex Standards Ltd.)	40	40
Mg	5	TAP	Hornblende (Kakanui) (NMNH 143965)	40	40
Ca	2	PETJ	Anorthite (NMNH 137041)	40	20
Na	5	TAP	Anorthoclase (NMNH 133868)	30	15
K	4	PETL	Microcline (NMNH 143966)	40	20
Ba	4	PETL	Corning Glass C (NMNH 117218-2)	40	40

Table S4.

Standards, spectrometers and analytical crystals used, and counting times on peak and background on each side of peak for plagioclase analyses.

Element	Spec.	Crystal	Standard	Peak (sec)	Backgr. (sec)
Si	1	TAP	Augite (NMNH 122142)	30	15
Ti	2	PETJ	Hornblende (Kakanui) (NMNH 143965)	30	30
Al	1	TAP	Pyrope (NMNH 143968)	30	15
Fe	3	LIFH	Hornblende (Kakanui) (NMNH 143965)	30	15
Mn	4	LIFL	Bustamite (Astimex Standards Ltd.)	30	30
Mg	5	TAP	Hypersthene (USNM 746)	30	15
Ca	2	PETJ	Diopside (NMNH 117733)	30	15
Na	5	TAP	Omphacite (NMNH 110607)	30	15
Cr	4	LIFL	Chromite (NMNH 117075)	30	15
Ni	3	LIFH	Pentlandite (Astimex Standards Ltd.)	30	30

Table S5.

Standards, spectrometers and analytical crystals used, and counting times on peak and background on each side of peak for clinopyroxene analyses.

Parameter	S1-D	S1-E	F1-D	F1-E	F2-D	F2-E
$^{87}Sr/^{86}Sr$	0.70309	0.70325	0.70309	0.70325	0.70309	0.70319
$^{143}Nd/^{144}Nd$	0.51304	0.51294	0.51304	0.51294	0.51304	0.51294
Sr ($\mu g\ g^{-1}$)	160	220	110	220	110	170
Nd ($\mu g\ g^{-1}$)	17	18	6	12	6	12

Table S6.

The parameters used in the mixing models shown in Figs. S26, S27A,B. The enriched endmembers are denoted with an "E" suffix, and the depleted endmembers are denoted with a "D" suffix. The S1 model is shown by the solid line in the figures. The F1 model is the dashed line in the figures. The F2 model is the dotted line in the figures.

Parameter	S-D	S-E	F-D	F-E
La (μg g^{-1})	4.0	13.71	2.0	8.26
Yb (μg g^{-1})	4.44	2.75	2.22	2.04
K_2O (wt%)	0.09	0.423	0.025	0.288
TiO_2 (wt%)	3.0	1.74	0.83	1.15

Table S7.

The parameters used in the mixing models shown in figs. S4C, S27B,C. The enriched endmembers are denoted with an "E" suffix, and the depleted endmembers are denoted with a "D" suffix. The S model is shown by the solid line in the figures. The F model is the dotted line in the figures.

Data S1. (separate file)
Sample information.

Data S2. (separate file)
Major oxide concentrations for the sample whole rocks and standard powders determined by ICP-OES.

Data S3. (separate file)
The data collected from glasses and minerals by electron microprobe analysis, including samples and standards.

Data S4. (separate file)
The trace element data collected by ICP-MS for both picked glasses from the samples and standard powders.

Data S5. (separate file)
The Sr and Nd radiogenic isotope analyses.